

Regulation of the pancreatic K_{ATP} channel

Samuel Usher

Green Templeton College
University of Oxford

*A thesis submitted for the degree of
Doctor of Philosophy*

Trinity 2021

Abstract

Regulation of the pancreatic K_{ATP} channel



Samuel Usher
Green Templeton College
University of Oxford

A thesis submitted for the degree of

Doctor of Philosophy

Trinity 2021

Acknowledgements

Abstract

Contents

List of Figures	ix
1 Introduction	1
1.1 General introduction	1
1.2 Structure and function of the pancreatic K _{ATP} channel	1
1.2.1 Pancreatic islets and the β-cell	1
1.2.2 Glucose induced insulin secretion in β-cells	2
1.2.3 Architecture of the pancreatic K _{ATP} channel	2
1.2.4 Nucleotide regulation of the pancreatic K _{ATP} channel	4
1.3 Fluorescence methods in ion channel research	5
1.3.1 Fluorescence as a tool	5
1.3.2 Forster resonance energy transfer	5
1.3.3 Unnatural amino acid incorporation	5
1.4 Functional modelling of ion channels	5
1.4.1 Why?	5
1.4.2 A model that fits	5
2 Methods	9
2.1 Molecular biology	9
2.2 Cell culture and channel expression	10
2.3 Western blots	11
2.4 Confocal microscopy	12
2.5 Surface expression assays	13
2.6 Epifluorescence imaging and spectroscopy	14
2.7 Electrophysiology	14
2.8 FRET calculations	15
2.9 Unroofed binding measurements	16
2.10 Patch-clamp fluorometry	17
2.11 Data processing and presentation	17
2.12 Computational docking	18
2.13 Chemicals and stock solutions	18

3 Measuring nucleotide binding to K_{ATP}	19
3.1 Designing a nucleotide binding assay	19
3.1.1 Criteria for a useful assay	19
3.1.2 Choosing a site to incorporate ANAP	21
3.2 Incorporating ANAP into the Kir6.2 binding site	25
3.2.1 Amber stop codon expression system	25
3.2.2 ANAP incorporation into amber stop codon containing constructs	25
3.3 Testing for functional membrane expression	26
3.3.1 Surface expression of HA-epitope labelled Kir6.2 constructs . .	26
3.3.2 Electrophysiology of Kir6.2 constructs	27
3.3.3 Unroofed membrane binding assay of Kir6.2 constructs	28
3.3.4 Patch-clamp fluorometry of Kir6.2 constructs	30
3.4 Discussion	31
4 MWC modelling	43
4.1 Modelling of ion channel function	43
4.1.1 Restricting the subset of possible models	43
4.1.2 Considerations for fitting a model	43
4.1.3 Determining open probability	43
4.2 Implementing an MWC model	49
4.2.1 A simple case	49
4.2.2 The role of PIP ₂	49
5 Nucleotide regulation of Kir6.2	55
5.1 Nucleotide binding	55
5.1.1 G334D abolishes nucleotide binding	55
5.2 Channel gating	55
5.2.1 C166S alters inhibition without affecting binding	55
5.2.2 Mutations at E179 alter both inhibition and binding	55
5.2.3 Mutations at K39 alter both inhibition and binding	55
5.3 Discussion	55
6 Regulation of Kir6.2 by SUR1	57
6.1 Intrinsic effects of SUR1	58
6.1.1 SUR1 alone alters nucleotide inhibition	58
6.1.2 Presence of SUR1 alone does not alter apparent nucleotide binding	58
6.1.3 Presence of SUR1-TMD0 alone does not alter apparent nucleotide binding	58
6.2 SUR1 an nucleotide regulation	58
6.2.1 Mutations at SUR-K205 alter nucleotide binding and inhibition	58
6.2.2 THe presence of magnesium does not affect nucleotide binding	58
6.3 Discussion	58

7 Discussion	59
---------------------	-----------

Appendices	
-------------------	--

X

List of Figures

1.1 Structure of Kir6.2	3
1.2 Structure of SUR1	5
1.3 K _{ATP} architecture and nucleotide regulation	6
1.4 SUR1 intrinsically modulates Kir6.2	7
3.1 Anap and TNP-nucleotides as FRET pairs	22
3.2 TNP-nucleotides can bind with a similar pose to ATP	24
3.3 ANAP incorporation	33
3.4 Confocal imaging	34
3.5 ANAP construct surface expression assay	35
3.6 WT-GFP and W311*-GFP electrophysiology	36
3.7 Unroofed membranes spectral images	37
3.8 Unroofed membranes bleaching correction	38
3.9 W311*-GFP unroofed membrane binding	39
3.10 PCF bleaching correction	40
3.11 ANAP is not quenched by ATP	41
4.1 Systematic underestimation of single channel currents	46
4.2 Estimating open probability from stationary noise analysis	48
4.3 Generating data from MWC model schemes	50
4.4 Parameter retrieval from MWC models	51
4.5 Parameter retrieval from MWC models	52

xii

1

Introduction

Contents

1.1 General introduction	1
1.2 Structure and function of the pancreatic K_{ATP} channel	1
1.2.1 Pancreatic islets and the β-cell	1
1.2.2 Glucose induced insulin secretion in β-cells	2
1.2.3 Architecture of the pancreatic K _{ATP} channel	2
1.2.4 Nucleotide regulation of the pancreatic K _{ATP} channel	4
1.3 Fluorescence methods in ion channel research	5
1.3.1 Fluorescence as a tool	5
1.3.2 Förster resonance energy transfer	5
1.3.3 Unnatural amino acid incorporation	5
1.4 Functional modelling of ion channels	5
1.4.1 Why?	5
1.4.2 A model that fits	5

1.1 General introduction

1.2 Structure and function of the pancreatic K_{ATP} channel

1.2.1 Pancreatic islets and the β-cell

Pancreatic islets are endocrine cells which are responsible for maintaining glucose homeostasis. There are roughly one million islets in a human pancreas, constituting

1-2% of the total pancreatic mass. Islets consist of three principal cell types; insulin secreting β -cells, glucagon secreting α -cells and somatostatin secreting δ -cells. Islets respond to increases in blood glucose by releasing insulin, which acts on peripheral tissues to increase glucose uptake and reduce blood glucose levels. Conversely, decreases in blood glucose leads to the release of glucagon, which acts on those tissues to stimulate glucose production and increase blood glucose.

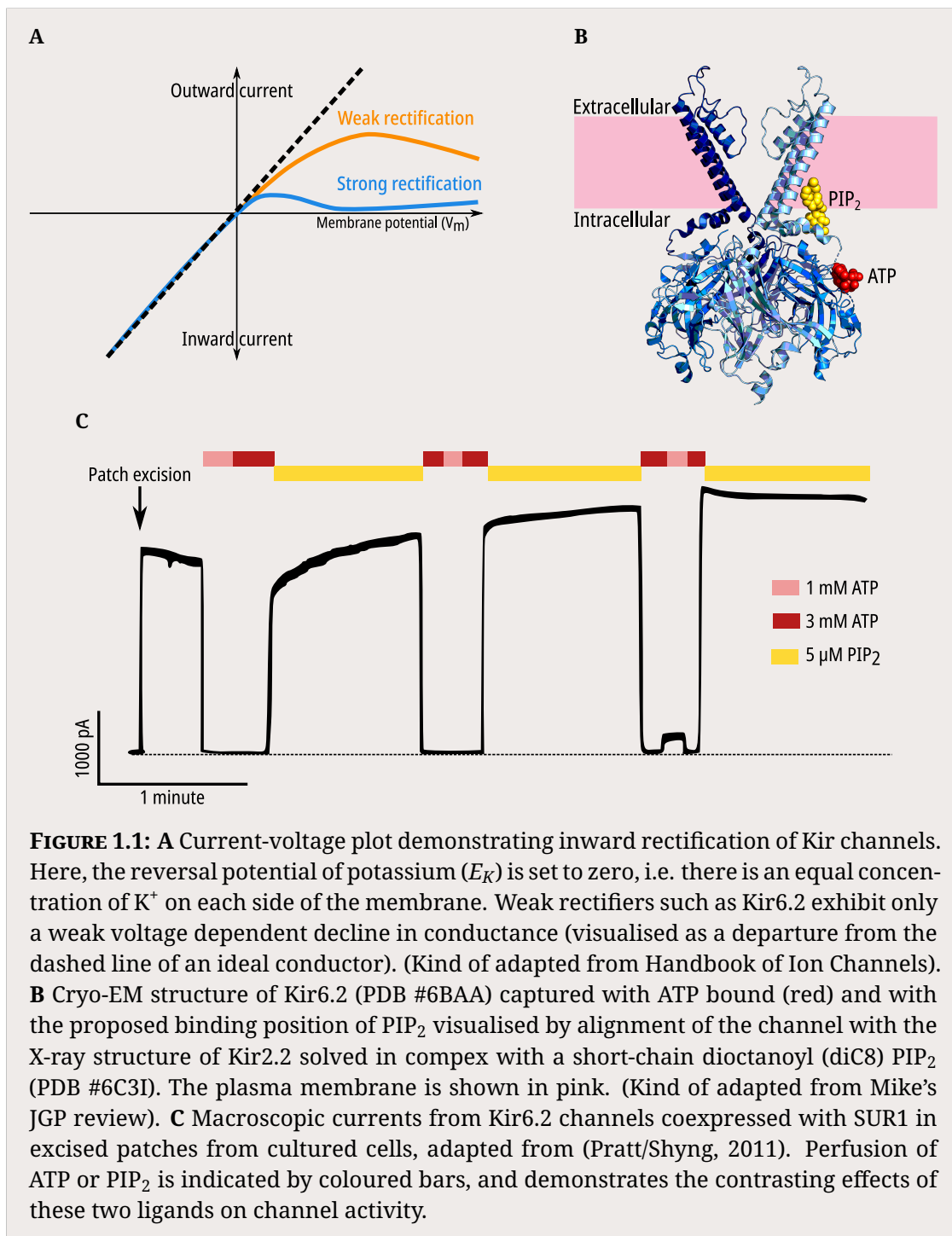
1.2.2 Glucose induced insulin secretion in β -cells

1.2.3 Architecture of the pancreatic K_{ATP} channel

ATP-sensitive potassium (K_{ATP}) channels are present in many tissues, where they couple the metabolic state of a cell to its electrical activity by regulating the flow of K⁺ across the membrane. K_{ATP} channels are an octameric complex, comprised of four inwardly-rectifying potassium channel subunits (Kir6.1 or Kir6.2), each of which is associated with a sulphonylurea receptor subunit (SUR1, SUR2A or SUR2B). In pancreatic β -cells, the K_{ATP} channel isoform is composed of Kir6.2 and SUR1.

Inwardly-rectifying potassium channels are so named because they allow K⁺ to flow more easily into the cell than out of it (Figure 1.1A). This phenomenon is a consequence of voltage-dependent pore blockade by intracellular divalent cations (especially Mg²⁺) and polyamines. At depolarising membrane potentials, blockers are driven into the pore and K⁺ current is blocked, while at hyperpolarising potentials the blockers are cleared and K⁺ current can flow. Strongly rectifying Kir channels display drastically reduced conductance at potentials more positive than the K⁺ reversal potential. In contrast, Kir6.2 is a weak rectifier, and allows substantial current to flow at more positive potentials.

In addition to voltage, Kir6.2 is regulated by two endogenous ligands; phosphatidylinositol 4,5-bisphosphate (PIP₂) and adenine nucleotides (Figure 1.1B). The binding of adenine nucleotides to Kir6.2 leads to closure of the channel pore, while the binding of PIP₂ promotes the opening of the pore (Figure 1.1C). Activation by PIP₂ is a mechanism common to the whole Kir family, whereas inhibition by nucleotides is unique to the Kir6 subfamily.



SUR1 is a member of the ATP-binding cassette (ABC) family of transporters. While other ABC proteins transport substrate across the membrane, SUR1 does not appear to do so; instead it acts to modulate the function of its associated ion channel. The cystic fibrosis transmembrane conductance regulator (CFTR) is another

member of the ABC family, and is an ion channel in its own right, capable of conducting chloride across the membrane. Like other ABC proteins, SUR1 contains two sets of transmembrane domains (TMD1 and TMD2) and two cytosolic nucleotide binding domains (NBD1 and NBD2). Unique to SUR is the presence of an additional transmembrane domain (TMD0) N-terminal to the core of the protein, and this domain forms the primary contact between SUR1 and Kir6.2.

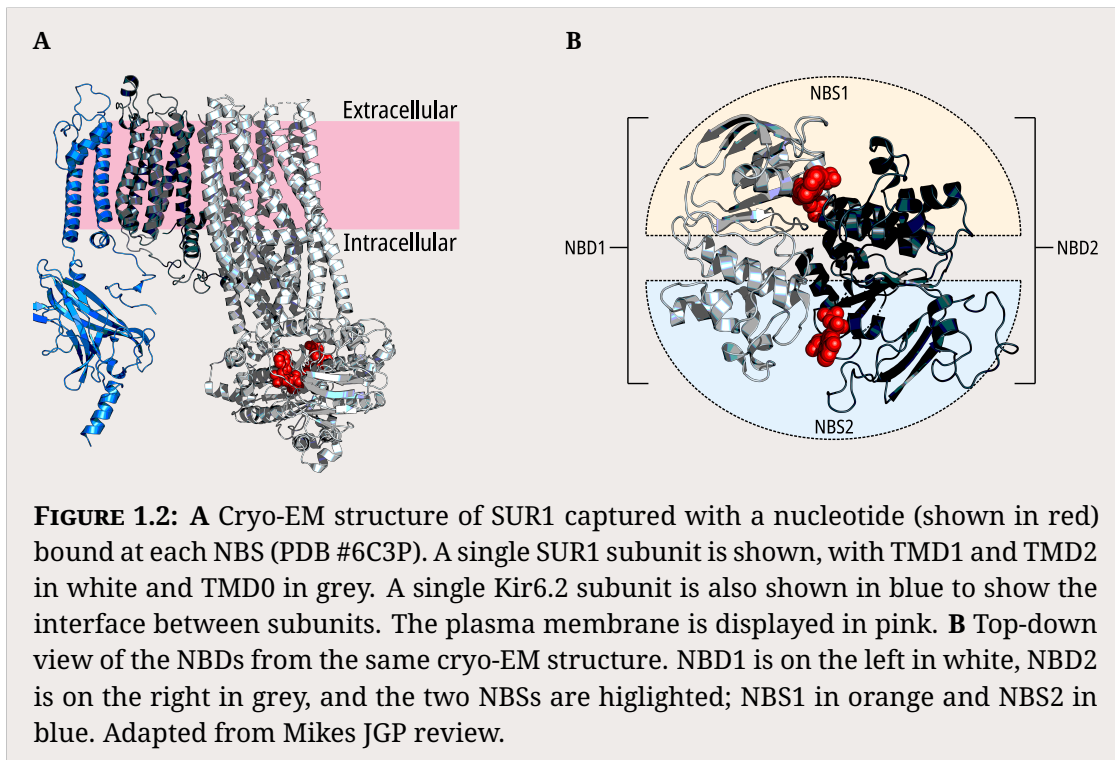
The NBDs of ABC transporters are highly conserved, and consist of two subdomains: a larger RecA-like subdomain found in other P-loop ATPases, and a smaller α -helical subdomain which is unique to ABC transporters. There are three key structural motifs present in these subdomains: the RecA-like subdomain contains the Walker A (W_A) and B (W_B) motifs, while the α -helical subdomain contains the ABC signature motif (typically LSGQQ).

The two domains come together to form an antiparallel dimer with two nucleotide binding sites (NBS1 and NBS2) at the interface, such that NBS1 is formed from the W_A and W_B motifs of NBD1 and the signature motif from NBD2, whereas NBS2 is formed from the W_A and W_B motifs of NBD2 and the signature motif from NBD1. NBS2, also known as the consensus site as it is more similar in sequence to other ABC family members, is catalytically competent and able to hydrolyse ATP. In contrast, NBS1 is the degenerate site, with a less conserved sequence and an inability to catalyse hydrolysis of ATP.

Sulphonylureas go here.

1.2.4 Nucleotide regulation of the pancreatic K_{ATP} channel

Together, Kir6.2 and SUR1 form a complex nearly a megadalton in size and over 15 nanometres across (Figure 1.3A, 1.3B). While the binding of adenine nucleotides to the Kir6.2 binding site leads to closure of the pore, binding of nucleotides to either of the two NBSs of SUR1 in the presence of Mg²⁺ activates the channel. The interplay between the action of nucleotides at these distinct sites (Figure 1.3C) determines the response of the K_{ATP} channel to metabolic changes, and therefore even subtle mutations or modifications to these sites can lead to diseases of insulin secretion.



In addition to its nucleotide binding and sensitivity to sulphonylureas, SUR1 also has intrinsic effects on channel properties. The presence of SUR1 increases the open probability of the channel pore (Figure 1.4A), and this increase is conferred by the TMD0 region (Figure 1.4B). Furthermore, coexpression of SUR1 increases the sensitivity of Kir6.2 to inhibition by nucleotides (Figure 1.4C).

1.3 Fluorescence methods in ion channel research

1.3.1 Fluorescence as a tool

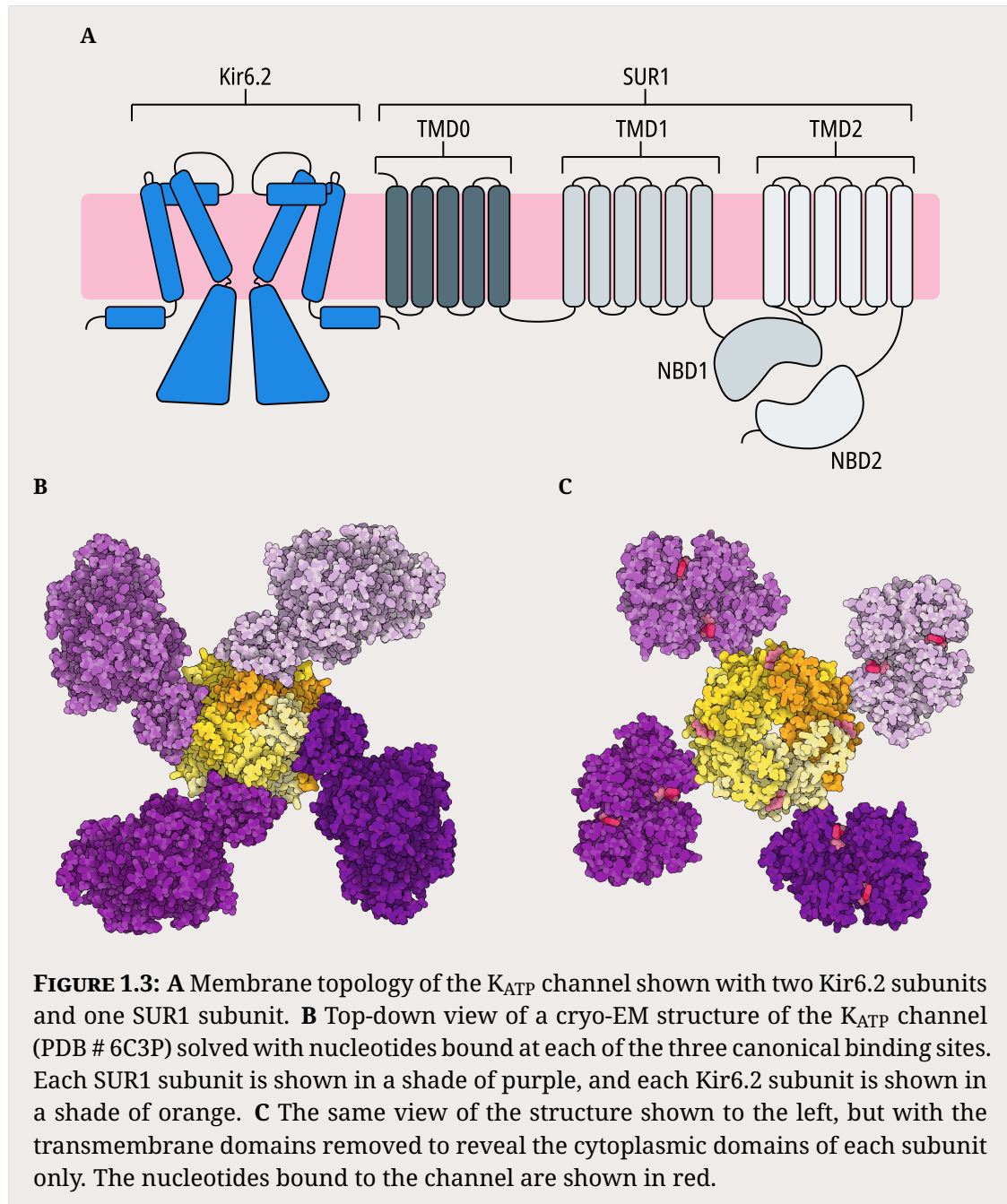
1.3.2 Forster resonance energy transfer

1.3.3 Unnatural amino acid incorporation

1.4 Functional modelling of ion channels

1.4.1 Why?

1.4.2 A model that fits



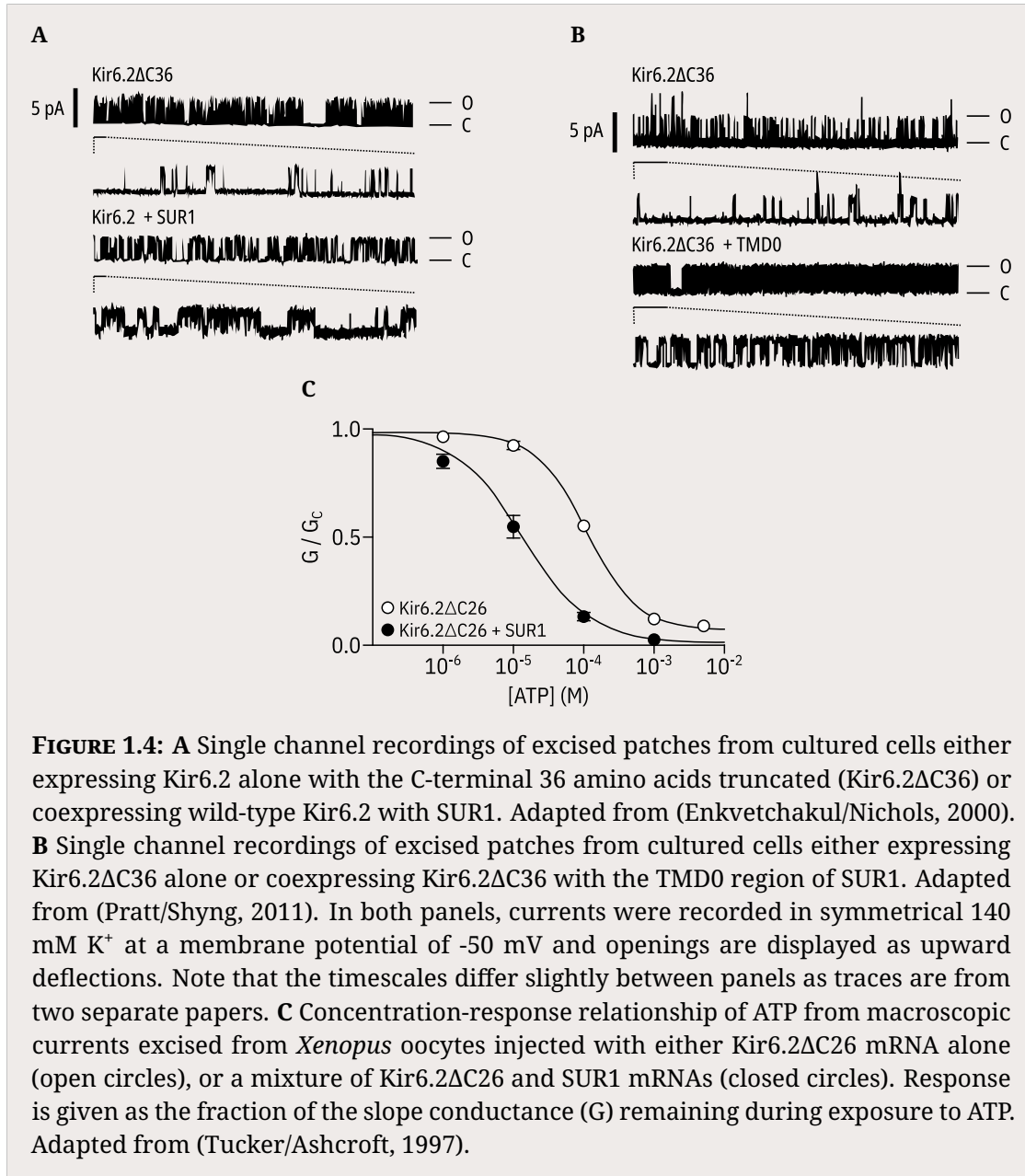


FIGURE 1.4: **A** Single channel recordings of excised patches from cultured cells either expressing Kir6.2 alone with the C-terminal 36 amino acids truncated (Kir6.2ΔC36) or coexpressing wild-type Kir6.2 with SUR1. Adapted from (Enkvetchakul/Nichols, 2000). **B** Single channel recordings of excised patches from cultured cells either expressing Kir6.2ΔC36 alone or coexpressing Kir6.2ΔC36 with the TMD0 region of SUR1. Adapted from (Pratt/Shyng, 2011). In both panels, currents were recorded in symmetrical 140 mM K⁺ at a membrane potential of -50 mV and openings are displayed as upward deflections. Note that the timescales differ slightly between panels as traces are from two separate papers. **C** Concentration-response relationship of ATP from macroscopic currents excised from *Xenopus* oocytes injected with either Kir6.2ΔC26 mRNA alone (open circles), or a mixture of Kir6.2ΔC26 and SUR1 mRNAs (closed circles). Response is given as the fraction of the slope conductance (G) remaining during exposure to ATP. Adapted from (Tucker/Ashcroft, 1997).

2

Methods

Contents

2.1 Molecular biology	9
2.2 Cell culture and channel expression	10
2.3 Western blots	11
2.4 Confocal microscopy	12
2.5 Surface expression assays	13
2.6 Epifluorescence imaging and spectroscopy	14
2.7 Electrophysiology	14
2.8 FRET calculations	15
2.9 Unroofed binding measurements	16
2.10 Patch-clamp fluorometry	17
2.11 Data processing and presentation	17
2.12 Computational docking	18
2.13 Chemicals and stock solutions	18

2.1 Molecular biology.

Human Kir6.2 and SUR1 were subcloned into pcDNA4/TO and pCGFP_EU vectors for expression of wild-type and GFP-tagged constructs, respectively. pcDNA4/TO and pANAP were obtained from Addgene. peRF1-E55D and pCGFP_EU were kind gifts from the Chin Laboratory (MRC Laboratory of Molecular Biology, Cambridge, UK) and the Gouaux Laboratory (Vollum Institute, Oregon, USA) respectively. Amber

stop codons and point mutations were introduced using the QuikChange XL system (Stratagene; San Diego, CA). All constructs were confirmed by DNA sequencing (DNA Sequencing and Services, University of Dundee, Scotland).

2.2 Cell culture and channel expression

HEK-293T cells were obtained from and verified/tested for mycoplasma by LGC standards (ATTC CRL-3216, Middlesex, UK). Our working stock tested negative for mycoplasma contamination using the MycoAlert Mycoplasma Detection Kit (Lonza Bioscience; Burton on Trent, UK). Cells were plated onto either poly-L-lysine coated borosilicate glass coverslips (VWR International; Radnor, PA) or poly-D-lysine coated glass-bottomed FluoroDishes (FD35-PDL-100, World Precision Instruments). ANAP-tagged Kir6.2 constructs were labelled using amber stop codon suppression as described by Chatterjee et al. Transfections were carried out 24 hours after plating using TransIT-LT1 (Mirus Bio LLC; Madison, WI) at a ratio of 3 µl per µg of DNA. Unless specified otherwise, all transfections included a Kir6.2 construct with an amber stop codon (TAG) at position 311 (Kir6.2-W311^{TAG}), SUR1, pANAP and eRF1-E55D in the ratio 0.5:1.5:1:1. Transfected cells cultured in Dulbecco's Modified Eagle Medium (Sigma; St. Louis, MO) + 10% foetal bovine serum, 100 U ml⁻¹ penicillin and 100 µg ml⁻¹ streptomycin (Thermo Fisher Scientific; Waltham, MA) supplemented with 20 mM ANAP (free acid, AsisChem; Waltham, MA). Cells were incubated at 33 °C and in the presence of 300 µM tolbutamide to enhance protein expression and channel trafficking to the plasma membrane. eRF1-E55D was included to increase efficiency of ANAP incorporation. Experiments were carried out 2-4 days after transfection. We also expressed constructs labelled with ANAP at positions I182, F183, F198, and I210. Kir6.2-F183*, Kir6.2-F198*, and Kir6.2-I210* co-expressed with SUR1 did not produce sufficient currents for subsequent experimentation. Mutations at I182 are known to produce profound effects on nucleotide inhibition of K_{ATP}. Thus, we did not consider this site for further experimentation.

2.3 Western blots

Transfected HEK-293T cells grown in 6-well plates were harvested in cold PBS (Life Technologies Limited; Paisley, UK), pelleted at 0.2 x g for 2.5 minutes and resuspended in lysis buffer containing 0.5% Triton X-100, 100 mM potassium acetate, and a cOmplete protease inhibitor tablet (1 tablet/50 ml, Roche; Basel, Switzerland), buffered to pH 7.4. After a 30-minute benzonase (Sigma) treatment at room temperature, samples were mixed with a DTT containing reducing agent and loading buffer (NuPAGE, Invitrogen; Carlsbad, CA) and run on a precast Bis-Tris 4-12% polyacrylamide gel at 200 V for 40 minutes. Proteins were wet transferred overnight onto polyvinylidene difluoride (PVDF) membranes (Immobilon P, Merck Millipore; Burlington, VT) in 25 mM Tris, 192 mM glycine, 20% methanol, and 0.1% SDS at 10 V on ice. Membranes were blocked with 5% milk in TBS-Tw (150 mM NaCl, 0.05% Tween 20, 25 mM Tris, pH 7.2) before staining for 30 minutes with a 1:1000 dilution of rat anti-HA monoclonal antibody in TBS-Tw (clone 3F10, Roche). After washing with TBS-Tw, membranes were incubated for 30 minutes with a 1:20,000 dilution of HRP-conjugated goat anti-rat polyclonal antibodies in TBS-Tw (Jackson ImmunoResearch; Ely, UK). Detection was performed using the SuperSignal West Pico Chemiluminescent Substrate (Thermo Fisher) and a C-DiGit Blot Scanner (Licor Biosciences; Lincoln, NE). Analysis was performed using custom code written in Python.

To confirm our ability to express full-length Kir6.2*-GFP, we performed western blots for HA-tagged Kir6.2 constructs in detergent-solubilized HEK-293T cells (Figure 1—Figure supplement 1C). The HA tag plus a short linker (YAYMEKGITDLAYPYD-VPDY) was inserted in the extracellular region following helix M1 of Kir6.2 between L100 and A101. Transfection of wild-type Kir6.2-HA or Kir6.2-HA-GFP resulted in two bands on the western blots. The upper bands were close to the expected sizes for full-length Kir6.2-HA and Kir6.2-HA-GFP (46 kDa and 77 kDa, respectively).

We consistently observed a lower molecular weight band as well. This band must correspond to an N-terminally truncated Kir6.2 product, as the apparent molecular weight shifted with addition of the C-terminal GFP tag. Based on the

molecular weight, we predict that the truncated protein product initiated from a start codon in the first transmembrane domain. Therefore, we believe it is unlikely that this protein would form functional channels or traffic to the plasma membrane. When Kir6.2-W311^{TAG}-HA or Kir6.2-W311^{TAG}-HA-GFP were co-transfected with SUR1, pANAP, and eRF1-E55D, and cells were cultured in the presence of ANAP, the western blots were similar to wild-type Kir6.2-HA or Kir6.2-HA-GFP. Over 90% full-length Kir6.2*-HA-GFP was produced under these conditions (Figure 1—Figure supplement 1D). We were unable to quantify the percentage of full-length Kir6.2*-HA produced as the C-terminally truncated band resulting from termination at the TAG codon was very similar in size to the N-terminally truncated band. Co-expression with SUR1 increased the percentage of full-length Kir6.2*-HA-GFP produced (Figure 1—Figure supplement 1D). In the absence of ANAP, we did not observe any full-length Kir6.2, indicating that there was no read-through of the amber (TAG) stop codon (Figure 1—Figure supplement 1D).

2.4 Confocal microscopy

Confocal imaging was performed using a spinning-disk system (Ultra-VIEW VoX, PerkinElmer; Waltham, MA) mounted on an IX81 microscope (Olympus; Southend-on-Sea, UK) with a Plan Apo 60x oil immersion objective (NA = 1.4), provided by the Micron Advanced Bioimaging Unit, Oxford. Transfected HEK-293T cells were incubated for 15 minutes with 1 nM CellMask Deep Red (Thermo Fisher) to stain plasma membranes before washing with PBS and imaging. ANAP was excited with a solid-state laser at 405 nM. GFP and CellMask were excited with an argon laser at 488 nM and 633 nM respectively. Images were captured on an EMCCD camera (ImagEM; Hamamatsu Photonics; Welwyn Garden City, UK) binned at 2 x 2 pixels and analysed using Python. A median filter with a box size of 32 x 32 pixels was applied to improve the signal-to-noise ratio by reducing background fluorescence.

We examined the surface expression of our ANAP-labelled constructs using confocal microscopy (Figure 1—Figure supplement 1A,B). When Kir6.2-W311^{TAG}-GFP was co-transfected with SUR1 along with pANAP and eRF1-E55D in the presence

of ANAP, the ANAP and GFP fluorescence were co-localized at the plasma membrane. When wild-type Kir6.2-GFP was transfected under the same conditions, only GFP fluorescence was observed at the plasma membrane. ANAP fluorescence was diffuse and confined to the cytoplasm or intracellular structures. Thus, the plasma-membrane ANAP signal was specific for Kir6.2*-GFP.

2.5 Surface expression assays

We measured surface expression of HA-tagged Kir6.2 subunits using an approach outlined by Zerangue et al. Cells were plated on 19 mm coverslips coated with poly-L-lysine and transfected as described above. Following incubation, cells were rinsed with PBS before fixation with 10% formalin for 30 minutes at room temperature. After washing again, cells were blocked with 1% BSA in PBS for 30 minutes at 4 °C before a 1-hour incubation at 4 °C with a 1:1000 dilution (in PBS) of rat anti-HA monoclonal antibodies. Cells were then washed 5 times on ice with 1% BSA in PBS followed by a 30-minute incubation at 4 °C with a 1:2000 dilution of HRP-conjugated goat anti-rat polyclonal antibodies. Cells were washed 5 times in PBS + 1% BSA and 4 times in PBS. Coverslips were removed from the culture dishes and placed in clean, untreated dishes for measurement. 300 µl of SuperSignal ELISA Femto Maximum Sensitivity Substrate (Thermo Fisher) was added to each sample and the luminescence was measured using a Glomax 20/20 Luminometer (Promega; Madison, WI) after a 10 second incubation.

HEK-293T cells were transfected with Kir6.2 constructs with or without a TAG stop codon corresponding to position 311. Cells were co-transfected with pANAP and eRF1-E55D in the presence or absence of SUR1 and cultured with or without ANAP. Wild-type Kir6.2-HA and Kir6.2-HA-GFP in the presence of SUR1 were included as positive controls. Kir6.2 constructs with no HA tag served as negative controls. In the presence of ANAP, we observed strong trafficking of Kir6.2*-HA-GFP to the plasma membrane, but much less trafficking of Kir6.2*-HA (Figure 1—Figure supplement 1E). When cells were cultured in the absence of ANAP, we observed little to no Kir6.2 surface expression from cells that were transfected with Kir6.2-W311^{TAG}-HA

or Kir6.2-W311^{TAG}-HA-GFP, suggesting that prematurely truncated constructs did not traffic to the plasma membrane. In the absence of SUR1, surface expression was weak for both wild-type and tagged constructs, despite the reported ability of Kir6.2-GFP to traffic to the plasma membrane in the absence of SUR1.

2.6 Epifluorescence imaging and spectroscopy

Epifluorescence imaging and spectroscopy were performed using a Nikon Eclipse TE2000-U microscope with a 60x water immersion objective (Plan Apo VC, NA = 1.2, Nikon; Kingston upon Thames, UK) or a 100x oil immersion objective (Nikon, Apo TIRF, NA = 1.49). Imaging of ANAP was performed using a 385 nm LED source (ThorLabs; Newton, NJ) with a 390/18 nm band-pass excitation filter, an MD416 dichroic and a 479/40 nm band-pass emission filter (all from ThorLabs). GFP was imaged using a 490 nm LED source (ThorLabs) with a 480/40 nm band-pass excitation filter, a DM505 dichroic, and a 510 nm long-pass emission filter (all from Chroma; Bellows Falls, VT). Fluorescence spectra were collected by exciting ANAP as above but using a 400 nm long-pass emission filter (ThorLabs), then passing emitted light through an IsoPlane 160 Spectrometer (Princeton Instruments; Trenton, NJ) with a 300 g mm⁻¹ grating. Images were collected with 1 s exposures on a Pixis 400BR_eXcelon CCD (Princeton Instruments).

2.7 Electrophysiology.

Patch pipettes were pulled from thick-walled borosilicate glass capillaries (GC150F-15, Harvard Apparatus; Holliston, MA) to a resistance of 1.5 MΩ to 2.5 MΩ when filled with pipette solution. Currents were recorded at -60 mV from excised inside-out patches using an Axopatch 200B amplifier equipped with a Digidata 1322A digitizer and using pClamp 10 software (Molecular Devices; San Jose, CA). Currents were low-pass filtered at 5 kHz and digitized at 20 kHz. The bath solution (intracellular) contained 140 mM KCl, 10 mM HEPES, 1 mM EDTA and 1 mM EGTA (pH 7.3 with KOH). The pipette solution (extracellular) contained 140 mM KCl, 10 mM HEPES

and 1 mM EDTA (pH 7.4 with KOH). All experiments were carried out in Mg²⁺-free conditions. Currents were leak corrected using the current remaining in bath solution containing 5 mM barium acetate at 60 mV, assuming a linear leak with a reversal potential of 0 mV. Inhibition was calculated and corrected for rundown by alternating test concentrations of nucleotide solution with nucleotide-free solution, then expressing the test currents as a fraction of the average of the control currents before and after the test solution as described previously.

2.8 FRET calculations

We calculated the expected FRET efficiency between ANAP incorporated at amino acid position 311 and a docked TNP-ATP molecule as described previously. The equivalency between FRET efficiency (measured as ANAP quenching) and nucleotide binding is based on two main assumptions. Firstly, we assume that the observed quenching from a bound nucleotide does not differ dramatically between open and closed states of the channel. As there is no open-state structure of K_{ATP}, we do not know exactly how much relative movement would occur between a bound TNP-ATP and Kir6.2-W311. However, based on cryo-EM structures of apo and nucleotide-bound Kir6.2 we do not expect to see a change in the distance between these two positions.

Secondly, we assume that the ANAP and TNP-ATP molecules on each subunit do not undergo energy transfer with those on other subunits to an extent which would dramatically change the observed quenching. At saturating TNP-ATP concentrations, where each ANAP-labelled site on Kir6.2 is occupied, FRET between ANAP and the closest acceptor will be kinetically favoured and the overall FRET efficiency will not be affected by cross-talk between neighbouring sites. In the limiting case, at low TNP-ATP concentrations, one would expect a large proportion of Kir6.2 tetramers (with four ANAP-labelled binding sites) bound to only a single TNP-ATP molecule. In this case, we expect a 4% overestimation of nucleotide binding as calculated using a numerical method to simulate a single TNP-ATP acceptor with multiple ANAP donors based on the distances calculated from our docking. This may have resulted

in our binding curves becoming artificially shallow at low concentrations. However, this difference is not significant in the context of our measurements as it is smaller than the observed error of our measurements at low TNP-ATP concentrations.

2.9 Unroofed binding measurements.

Unroofed membranes were prepared as described previously. A coverslip plated with transfected HEK-293T cells was removed from the culture media and rinsed with PBS. The coverslip was then briefly sonicated using a probe sonicator (Vibra-cell; Newtown, CT) leaving behind adherent plasma membrane fragments. Cells cultured on FluoroDishes were rinsed and sonicated directly in the dish. Unroofed membrane fragments were nearly invisible in bright-field images and identified by their GFP and ANAP fluorescence. Fluorescent TNP-nucleotides (Jena Bioscience; Jena, Germany) were diluted in bath solution and perfused onto unroofed membranes using a valve controlled microvolume superfusion system (μ Flow, ALA Scientific Instruments; Farmingdale, NY).

Fluorescence spectra were collected as described above. A region of interest corresponding to the membrane fragment was manually selected and line-averaged for each wavelength. A similarly sized region of background was selected and averaged, then subtracted from the spectrum of interest. After subtraction, ANAP intensity was calculated by averaging the fluorescence intensity measured between 469.5 nm and 474.5 nm. Bleaching was corrected by fitting the normalised ANAP intensity of exposures taken during perfusion with nucleotide-free solution to a single exponential decay of the form

$$\frac{F}{F_{max}} = ae^{kt} + (1 - a) \quad (2.1)$$

then using the fit to correct the intensity of exposures taken during perfusion with test nucleotide solutions.

Some experiments were excluded from further analysis due to obvious cross-contamination between different solutions within the μ Flow superfusion system.

These were identified by noticeable colour changes in the solution in the delivery tubes.

2.10 Patch-clamp fluorometry.

The tip of the patch pipette was centred on the slit of the spectrometer immediately after patch excision. Currents were measured as described above. Fluorescence emission spectra from the excised patch were acquired concurrently with current measurements, both during test solution application as well as nucleotide-free solution. Background subtraction was slightly imperfect due to the exclusion of TNP-ATP from volume of the glass of the pipette, resulting in spectra that have negative intensities at the TNP-ATP peak at high nucleotide concentrations. However, this over-subtraction does not affect the size of the ANAP peak, which we used to quantify nucleotide binding.

Some experiments were excluded from further analysis due to low fluorescence intensity, as we were concerned about a low signal to noise ratio influencing our results.

2.11 Data processing and presentation.

Raw spectrographic images and current traces were pre-processed in Python and Clampfit (Axon) before analysis with R. Where applicable, all experimental data points are displayed in each figure. The number of experiments is reported in the figure legends and tables. To help visualise uncertainty and prevent some data points being hidden, they are arranged with a small amount of horizontal jitter; vertical position remains unaffected. Unless otherwise stated, summary statistics are overlaid as the mean with error bars representing the standard error of the mean. Where these error bars are not visible, they are smaller than the size of the point used for the mean.

Hill fits to fluorescence quenching were nonlinear least-squares fits to the following equation:

$$\frac{y}{y_{max}} = 1 - E_{max} + \frac{E_{max}}{1 + 10^{(EC_{50} - [TNPATP]) \cdot h}} \quad (2.2)$$

where y represents normalised fluorescence intensity and EC_{50} and $[TNPATP]$ are \log_{10} values. Current inhibition data were fit to the same equation but with y representing normalised current magnitude, IC_{50} instead of EC_{50} , and I_{max} instead of E_{max} .

2.12 Computational docking.

Computational docking of TNP-ATP into the nucleotide binding site of Kir6.2 was performed using AutoDock-Vina and Pymol (Schrödinger, LLC; New York, NY). 11 TNP-ATP structures from the Protein Data Bank (PDB accession #s 1I5D, 3AR7, 5NCQ, 5SVQ, 5XW6, 2GVD, 5A3S, 2PMK, and 3B5J) were used as starting poses and a 15x11.25x15 Å box was centred on the ATP bound to Kir6.2 in PDB accession #6BAA. Protonation states for each residue were assigned using PDB2PQR and PROPKA 3.0. The modal highest-scoring pose from the docking run was selected (PDB accession #5XW6) and distances were measured from a pseudo atom at the centre of the fluorescent moiety. TNP-ATP (PDB #3AR7) was positioned into the first nucleotide binding domain of SUR1 (PDB #6PZI) using the alignment tool in Pymol.

2.13 Chemicals and stock solutions.

Unless otherwise noted, all chemicals were obtained from Sigma. TNP-ATP was obtained as a 10 mM aqueous stock from Jena Bioscience and stored at -20°C . 1 mM aqueous stocks of ANAP-TFA were prepared by dissolving the free acid in 30 mM NaOH, and were stored at -20°C . Tolbutamide stocks (50 mM) were prepared in 100 mM KOH and stored at -20°C .

3

Measuring nucleotide binding to K_{ATP}

Contents

3.1 Designing a nucleotide binding assay	19
3.1.1 Criteria for a useful assay	19
3.1.2 Choosing a site to incorporate ANAP	21
3.2 Incorporating ANAP into the Kir6.2 binding site	25
3.2.1 Amber stop codon expression system	25
3.2.2 ANAP incorporation into amber stop codon containing constructs	25
3.3 Testing for functional membrane expression	26
3.3.1 Surface expression of HA-epitope labelled Kir6.2 constructs .	26
3.3.2 Electrophysiology of Kir6.2 constructs	27
3.3.3 Unroofed membrane binding assay of Kir6.2 constructs . .	28
3.3.4 Patch-clamp fluorometry of Kir6.2 constructs	30
3.4 Discussion	31

3.1 Designing a nucleotide binding assay

3.1.1 Criteria for a useful assay

Previous approaches to measuring nucleotide binding directly have relied on isolating binding to individual classes of site by disrupting protein function; either by introducing mutations which abolish binding to a particular site or by measuring binding to Kir6.2 or SUR1 alone. Traditionally, assays such as radioligand binding

experiments require purifying the protein out of its native membrane environment, thus rendering the channels nonfunctional.

To improve on these methods, an ideal assay measuring nucleotide binding to the K_{ATP} channel needs to fulfill a number of criteria.

1. We need sufficient spatial sensitivity to distinguish between different classes of binding site; i.e. the assay should be capable of distinguishing binding to Kir6.2 from binding to NBS1 or NBS2.
2. We should be able to measure binding to a functional channel, for which we need to be able to measure binding in a membrane.
3. There should be minimal perturbation of the channel in order for binding measurements to be physiologically relevant.

TO fulfill these criteria, we used an approach involving a fluorescent unnatural amino acid, ANAP. ANAP has been used increasing widely in the study of ion channel structure and function due to a few desirable qualities.

1. It is smaller than traditional fluorescent labels such as fluorescent proteins or rhodamine derivatives. Therefore, it should be less perturbing to the function of the protein it labels.
2. As it is an amino acid, it can be site-specifically inserted into any protein. This avoids the issues of other small chemical dyes which are targeted to a site via post-translational covalent modifications, typically by reacting with a cysteine residue. While this can be avoided in some proteins by mutating each cysteine residue to an alternative residue to avoid off-target labelling, there are functionally important cysteines in the K_{ATP} channel which cannot be mutated.
3. ANAP is environmentally sensitive, which has been used to great effect in other studies. Notably, the peak emission ranges from ~450nm to ~490nm depending on the hydrophobicity of the surrounding environment.

Initially, we hoped that the environmental sensitivity of ANAP fluorescence might be sufficient for the peak fluorescence of an ANAP residue inserted into an ATP binding site to measureably change when ATP was bound. Unfortunately, when we introduced ANAP directly into the Kir6.2 binding site in place of residues I182 or F183 we were not able to observe any functional K_{ATP} channels at the cell membrane.

Instead, we turned to FRET as a reporter for ATP binding. As ATP itself is not fluorescent, and has no intrinsic fluorescence quenching, we identified trinitrophenyl (TNP) -ATP as a fluorescent congener (Figure 3.1A). TNP-ATP is most commonly used as an antagonist of P2X receptors, which are also sensitive to endogenous ATP. TNP-ATP is an excellent FRET partner of ANAP, as evidenced by the good overlap in the TNP emission spectra and the ANAP extinction spectra (Figure 3.1B). This leads to a theoretical distance-dependency of FRET which is most sensitive between 20 Å to 60 Å (Figure 3.1C) with a calculated R_0 of 38.4 Å.

3.1.2 Choosing a site to incorporate ANAP

The theoretical R_0 of 38.4 Å for FRET between ANAP and TNP-ATP allowed for flexibility when choosing a site to incorporate ANAP. Ideally, a residue should be chosen to maximise the following aims:

1. The incorporated ANAP needs to be close enough to the nucleotide binding site of interest to report a quantifiable change in FRET when TNP-ATP is bound. This would not have to be close enough for 100 % FRET to occur, but the greater the efficiency achieved the higher the signal-to-noise ratio would be for measuring binding.
2. It also needs to be far enough from each other class of nucleotide binding site to avoid quenching by TNP-ATP bound to other sites.
3. In addition to avoiding interference from other classes of binding site, we also need to avoid cross-talk between nucleotide binding sites of the same class on different subunits, as this would lead to difficulty interpreting the measured quenching. The ideal theoretical solution would be labelling only

3.1. Designing a nucleotide binding assay

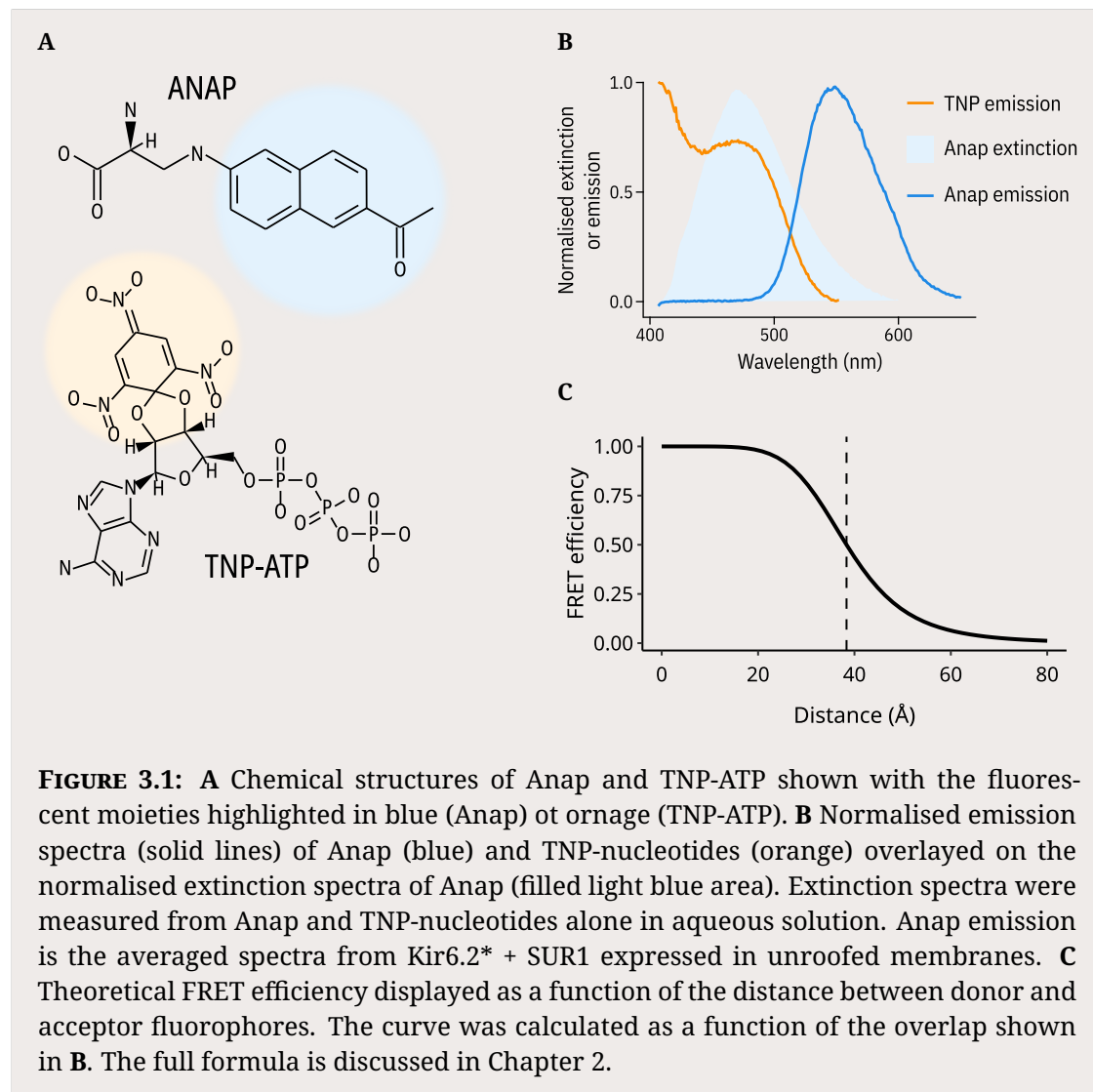


FIGURE 3.1: A Chemical structures of Anap and TNP-ATP shown with the fluorescent moieties highlighted in blue (Anap) or orange (TNP-ATP). B Normalised emission spectra (solid lines) of Anap (blue) and TNP-nucleotides (orange) overlayed on the normalised extinction spectra of Anap (filled light blue area). Extinction spectra were measured from Anap and TNP-nucleotides alone in aqueous solution. Anap emission is the averaged spectra from Kir6.2* + SUR1 expressed in unroofed membranes. C Theoretical FRET efficiency displayed as a function of the distance between donor and acceptor fluorophores. The curve was calculated as a function of the overlap shown in B. The full formula is discussed in Chapter 2.

one nucleotide binding site per ion channel, but without using a concatemer this is not so easy in practise.

To narrow down which residues could be candidates for ANAP incorporation to measure binding at Kir6.2, we took three cryo-EM structures of K_{ATP} with ATP bound and computationally docked TNP-ATP into the nucleotide binding pocket (Figure 3.2). To assess the validity of computationally docking a ligand to each structure, we first attempted to dock ATP to check that the highest-scoring binding poses were similar to those observed in the cryo-EM structures. Docking ATP to both #6C3P and #6C3O yielded binding poses which were very similar to the pose found in the

cryo-EM structures (Figures 3.2B, 3.2C). However, docking ATP to #6BAA resulted in binding poses which were in a flipped orientation relative to the pose found in the cryo-EM structure (Figure 3.2A).

We then took TNP-nucleotide structures from eleven different X-ray diffraction and cryo-EM structures published on RCSB to dock to the Kir6.2 binding site of K_{ATP} . For both #6BAA and #6C3P we observed that the three highest scoring binding poses for TNP-nucleotides closely resemble those of the ATP solved in complex with the channel (Figures 3.2A, 3.2B). It is not so clear for #6C3O, for which the highest scoring poses are not in agreement with each other or the solved structure of ATP.

Based on the predicted TNP-ATP poses for #6BAA and #6C3P, we could narrow down potential ANAP incorporation sites to within 25 Å of the centre of the TNP-moiety, at which distance we would expect to see over 90 % FRET efficiency when TNP-ATP is bound to Kir6.2. In addition, we excluded residues which fell within 45 Å of NBS1 or NBS2, as this restricts the potential FRET between TNP-ATP bound at these sites and our chosen residue to roughly 25 % or less. While we can exclude residues which fall too close to the NBS's of SUR1, the close proximity of the Kir6.2 nucleotide binding sites to each other means that we cannot exclude intersubunit FRET occurring; i.e. TNP-ATP binding to a neighbouring subunit will also be able to quench ANAP to a certain extent. However, this occurs in a predictable way that we can measure and account for.

We targeted two residues which fulfilled these criteria; F183 and W311. In addition, they are both bulky hydrophobic residues similar to ANAP, and at which no mutations have been previously identified to alter K_{ATP} function. To determine the extent to which crosstalk between neighbouring subunits would affect the measured FRET efficiency at these sites, we simulated the expected FRET for a single K_{ATP} channel bound to 0-4 molecules of TNP-ATP in an idealised scenario with no crosstalk, and compared the observed fluorescence quenching to a scenario including the possibility of crosstalk (Figure 3.2F). Due to the much shorter fluorescence lifetime of TNP-ATP compared to ANAP, we observe a deviation from the ideal scenario.

3.1. Designing a nucleotide binding assay

We can correct for this systematic deviation by transforming our observed ANAP

quenching (F/F_{max}) into $\log_2(\frac{F}{F_{max}+1})$.

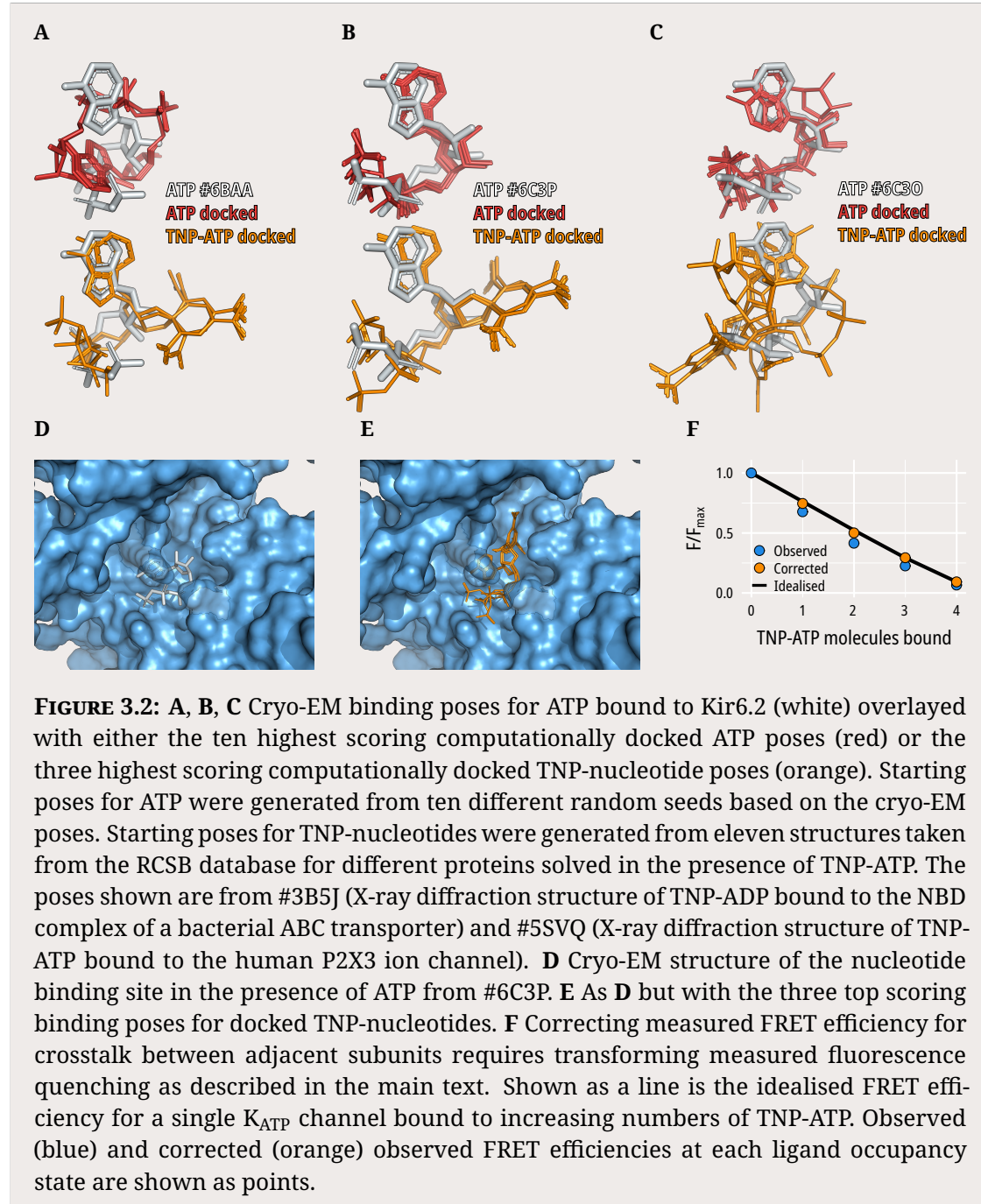


FIGURE 3.2: A, B, C Cryo-EM binding poses for ATP bound to Kir6.2 (white) overlaid with either the ten highest scoring computationally docked ATP poses (red) or the three highest scoring computationally docked TNP-nucleotide poses (orange). Starting poses for ATP were generated from ten different random seeds based on the cryo-EM poses. Starting poses for TNP-nucleotides were generated from eleven structures taken from the RCSB database for different proteins solved in the presence of TNP-ATP. The poses shown are from #3B5J (X-ray diffraction structure of TNP-ADP bound to the NBD complex of a bacterial ABC transporter) and #5SVQ (X-ray diffraction structure of TNP-ATP bound to the human P2X3 ion channel). D Cryo-EM structure of the nucleotide binding site in the presence of ATP from #6C3P. E As D but with the three top scoring binding poses for docked TNP-nucleotides. F Correcting measured FRET efficiency for crosstalk between adjacent subunits requires transforming measured fluorescence quenching as described in the main text. Shown as a line is the idealised FRET efficiency for a single K_{ATP} channel bound to increasing numbers of TNP-ATP. Observed (blue) and corrected (orange) observed FRET efficiencies at each ligand occupancy state are shown as points.

3.2 Incorporating ANAP into the Kir6.2 binding site

3.2.1 Amber stop codon expression system

ANAP can be introduced into a protein of interest by essentially expanding the genetic code to incorporate a noncanonical amino acid. The amber stop codon (TAG) is the least frequently occurring stop codon in eukaryotic cells, and can be repurposed to encode ANAP. An orthologous set of tRNA and its aminoacyl-tRNA synthetase are mutated and screened through directed evolution in order to charge the tRNA which recognises the amber stop codon with ANAP. Thus, in cells expressing the ANAP charged tRNA, the amber stop codon introduced into the protein of interest is suppressed and ANAP is translated instead (Figure 3.3A).

3.2.2 ANAP incorporation into amber stop codon containing constructs

The nature of the amber stop codon suppression system requires a number of careful controls to ensure the following:

1. Stop codon recognition is not perfect, and there is a chance of read-through. Instead of incorporating ANAP, it is possible that the translation machinery can insert endogenous amino acids instead, leading to production of full length, unlabelled Kir6.2. However, we found that cells transfected with W311TAG constructs and pANAP which were not cultured in the presence of ANAP did not produce full length Kir6.2 (Figure 3.3B, 3.3C), suggesting there is minimal read-through of the stop codon in our experiments.
2. Introducing a stop codon creates a risk that truncated Kir6.2 will be produced instead of ANAP labelled Kir6.2. This risk can be reduced by transfecting a dominant negative engineered version of eukaryotic translation termination factor 1(eRF1-E55D), which does not efficiently terminate protein synthesis in response to the amber stop codon (but leaves opal and ochre stop codons nearly unaffected) and thus increases the incorporation of ANAP. We found

that transfection of W311TAG constructs with a C-terminal GFP tag produced minimal truncated Kir6.2 (less than 10 % of the total density observed in Figure 3.3C).

3. Despite being the least frequent eukaryotic stop codon, the amber stop codon is still present in a significant number of protein sequences. We must be careful that ANAP is not incorporated into a protein which localises to the plasma membrane to an extent which would affect our ability to assign ANAP fluorescence to Kir6.2. We found that in cells transfected with GFP-tagged Kir6.2 without an amber stop codon, there was no increase in ANAP fluorescence at the cell membrane (Figure 3.4A, 3.4B). By contrast, when W311TAG-GFP was transfected, we saw a clear increase in ANAP fluorescence at the cell membrane (Figure 3.4C, 3.4D), suggesting that any observed ANAP fluorescence at the cell membrane originates from our labelled Kir6.2 construct.

3.3 Testing for functional membrane expression

3.3.1 Surface expression of HA-epitope labelled Kir6.2 constructs

To assess the ability of ANAP-incorporating constructs to traffic to the plasma membrane, we used a luminescence-based surface expression assay. This assay relies on the recognition of an HA-epitope introduced into an extracellular region of the protein of interest (in this case, the N-terminal region of Kir6.2) by an anti-HA primary antibody followed by an HRP-conjugated secondary antibody. The luminescence after applying HRP substrate is then proportional to the amount of protein at the plasma membrane of the cells.

We assessed the membrane expression of N-terminally HA-tagged Kir6.2 (nHA-Kir6.2) in the presence or absence of ANAP in the culture media and in the presence or absence of cotransfected SUR1. We also measured how the addition of a C-terminal GFP tag affected membrane expression under these conditions. We used untagged Kir6.2 as a control for nonspecific luminescence.

We find that for wild-type Kir6.2 (WT) there is roughly a 20-fold increase in observed luminescence when coexpressed with SUR1 over background, and roughly a 100-fold increase for the C-terminally GFP tagged Kir6.2 (WT-GFP, Figure 3.5A, 3.5C). There is no difference in surface expression of these constructs when ANAP is present in the culture medium (Figure 3.5A, 3.5D). When ANAP is incorporated at either residue 183 or 311 (F183* and W311* respectively) we see an increase in luminescence over background when coexpressed with SUR1 and with ANAP present in the culture medium (Figure 3.5A, 3.5C). The presence of the C-terminal GFP tag increases luminescence further for both constructs, dramatically so for W311*. However, when F183* is transfected and ANAP is not present in the culture media we still see a similar increase in fluorescence over background when compared to the luminescence when ANAP is present (Figure 3.5A, 3.5D), suggesting that a large proportion of the protein reaching the membrane does not have ANAP incorporated. In contrast, when W311*-GFP is transfected with SUR1 in the presence of ANAP, we see a 10-fold increase in luminescence compared to when ANAP is not present, consistent with the majority of surface expressed protein incorporating ANAP. We also see a consistent increase in luminescence for all constructs aside from W311* due to cotransfection with SUR1 (Figure 3.5B), suggesting that the incorporation of ANAP and the addition of a C-terminal GFP tag do not affect the role of SUR1 in forming the full K_{ATP} complex and trafficking to the membrane.

3.3.2 Electrophysiology of Kir6.2 constructs

To establish whether W311*-GFP formed K_{ATP} channels with similar function to wild-type, we excised patches from cells transfected with either WT-GFP or W311*-GFP cotransfected with SUR1. Excision was performed in Mg^{2+} -free solution to reduce rundown and to prevent activation of the channel by nucleotides. We observed similar magnitudes of current for both WT-GFP and W311*-GFP, and currents ran own at similar rates.

We fit our full dataset with equation 2.2 (Figure 3.6A), and used the estimated h and I_{max} parameters to fit each individual experiment and determine an IC_{50} value

(plotted as points in Figure 3.6C). The IC_{50} values were fit with a random effects model with values grouped by construct and nucleotide. The posterior probability distributions of this model are also shown in Figure 3.6C. These distributions reflect the variability of the observed data, not our uncertainty of the underlying IC_{50} value; i.e. we would expect 95 % of all future observations for a given construct and nucleotide to fall within the 95 % intervals of the distributions. For all IC_{50} and EC_{50} values fitted this way, in the text we will report the 95 % confidence intervals of the parameter estimate, which reflects only our uncertainty of the true value and not experimental variability.

Perfusion of ATP resulted in current inhibition with an IC_{50} of 25 μM to 45 μM for WT-GFP and 77 μM to 130 μM for W311*-GFP. Thus, despite the distance from the ATP binding site, the W311 mutation clearly affects some aspect of nucleotide inhibition. However, we assume that insights into the function of the ANAP-incorporating channel will still be applicable to wild-type channels despite the change in nucleotide inhibition.

Next, we established that TNP-ATP inhibits K_{ATP} to a similar extent as ATP (Figure 3.6B, 3.6D). We observed current inhibition with an IC_{50} of 0.7 μM to 1.8 μM for WT-GFP and 3.5 μM to 10 μM for W311*-GFP. K_{ATP} thus appears to be more sensitive to inhibition by TNP-ATP than by ATP. This could potentially be due to extra contacts made by the TNP moiety with Kir6.2, seen in our computational docking (Figure 3.2).

3.3.3 Unroofed membrane binding assay of Kir6.2 constructs

We then directly measured nucleotide binding to W311*-GFP in unroofed membranes. Briefly sonicating transfected cells adhered to coverslips results in the lower membrane of the cell remaining stuck to the coverslip while the rest of the cell contents is disrupted and perfused away. This leaves the cytoplasmic domains of expressed K_{ATP} channels open to perfusion of TNP-ATP. These patches of membrane are barely visible under brightfield illumination, but due to the presence of the C-terminal GFP tag and the incorporated ANAP, we can see patches of membrane expressing K_{ATP} channels light up when we excite either fluorophore (Figure 3.7A).

By measuring the fluorescence spectra of patches of unroofed membrane, we can separate the fluorescence emission peaks of the C-terminal GFP tag and the incorporated ANAP (Figure 3.7B). The peak at 472 nm corresponds to ANAP emission, while the peak at 508 nm corresponds to GFP emission. We observed no change in the locations of those peaks in the presence of ATP or TNP-ATP.

Perfusing TNP-ATP results in a decrease in the peak corresponding to ANAP fluorescence, and a concomitant increase in a fluorescence peak which corresponds to the TNP-ATP (Figure 3.7C). This phenomenon is the result of FRET between TNP-ATP bound to the channel at the Kir6.2 binding site. The decrease in ANAP fluorescence is almost directly correlated to an increase in bound nucleotide. We can plot the quenching of ANAP fluorescence as a concentration-response curve as in Figure 3.7D.

Before analysis, ANAP bleaching was corrected as shown in Figure 3.8A. ANAP intensities of spectra imaged during bath perfusion in between applications of TNP-ATP were fit with Equation 2.1. We found that all unroofed experiments showed bleaching well described by the single exponential fit to equation 2.1. In each experiment, there was a reasonable proportion of ANAP fluorescence remaining by the last exposure (Figure 3.8C), maintaining a good signal-to-noise ratio for each spectra imaged.

To equivocate ANAP quenching and nucleotide binding, first we need to adjust for the FRET between adjacent subunits of Kir6.2. The difference between the ideal 1:1 subunit/ligand FRET efficiency and the simulated experimental FRET efficiency resulted in a correction factor of $\log_2(\frac{F}{F_{max}} + 1)$.

Secondly, we need to correct for incomplete FRET due to the distance between the donor and acceptor. Based on the computational docking, we predicted a maximal FRET efficiency of 91 % when every Kir6.2 subunit is bound by TNP-ATP. Fitting our adjusted data to a Hill equation results in a maximum observed FRET efficiency of 90 %, agreeing well with our prediction. We can then normalise our observed fluorescence data by this value.

Overall, these two corrections do not dramatically alter our results (Figure 3.9A), and we performed our analysis on both corrected and uncorrected results to ensure that there was no potential difference in interpretation which derived from treating our data in this way.

We observed quenching of ANAP fluorescence over a concentration range of TNP-ATP similar to the range in which we observed inhibition of current in W311*-GFP (Figure 3.9B, 3.9C). When fit to a Hill equation, quenching was fit with an EC₅₀ of 21 µM to 31 µM, while the corrected binding data gave an EC₅₀ of 30 µM to 46 µM. Notably, this EC₅₀ is somewhat right-shifted compared to the IC₅₀ we observed in excised patches (3.5 µM to 10 µM).

3.3.4 Patch-clamp fluorometry of Kir6.2 constructs

To ensure that the ANAP fluorescence we observe in the unroofed membranes is emitted by functional channels, and thus the quenching by TNP-ATP reflects nucleotide binding to the same population of channels we are measuring inhibition from, we measured fluorescence quenching and current inhibition from the same excised patches (Figure 3.11A, 3.11B, 3.11C).

This experimental paradigm leads to two complications compared to performing the measurements separately. Firstly, the number of channels in an excised patch are far smaller than the number of channels in an unroofed membrane patch. This results in a much dimmer fluorescence readout, and a lower signal-to-noise ratio. Secondly, the presence of the pipette glass in the images results in some abnormalities in the background subtraction procedure. This is not due to the glass itself, but results from the occlusion of TNP-ATP from the image surrounding the patch. This leads to oversubtraction of the background TNP-ATP spectra, leading to an apparent negative peak in our corrected images. However, we find that there is no overlap of this peak and the ANAP peak, so our fluorescence quenching measurements are unaffected by this phenomenon. We were able to correct for ANAP bleaching in the same manner as we did for unroofed membranes (Figure 3.10).

Our fluorescence measurements from excised patches agree reasonably well (albeit slightly right-shifted) with our measurements for unroofed membranes (Figure 3.11D), with an EC_{50} value of $77 \mu\text{M}$ to $140 \mu\text{M}$. Our finding that the EC_{50} for TNP-ATP binding is right-shifted compared to the IC_{50} for TNP-ATP inhibition is consistent between each experimental paradigm (Figure 3.9B, 3.11E). This finding has implications for how exactly the binding of nucleotides to Kir6.2 leads to closure of the K_{ATP} channel pore.

3.4 Discussion

We have demonstrated that we can measure nucleotide binding to the inhibitory nucleotide binding site of Kir6.2 in intact, functional K_{ATP} channels in their native membrane environment. Measuring binding directly in either unroofed membrane patches or in excised patches simultaneously with current recordings reveals that nucleotide binding is right-shifted compared to nucleotide inhibition; i.e. K_{ATP} channels begin to close at nucleotide concentrations where there is very little binding. This observation rules out certain models of ion channel function, which will be explored further in chapter ??.

These findings come with some important caveats. Firstly, the introduction of ANAP into Kir6.2 at residue 311 clearly impacts nucleotide inhibition of the channel, increasing the observed IC_{50} values for ATP. Our analysis of nucleotide binding and inhibition is therefore predicated on this decrease in sensitivity to ATP inhibition not reflecting a disruption of the normal physiological mechanism of ATP inhibition. As all of our binding experiments are performed in the W311* background by necessity, we hope that measurements of relative changes in binding and inhibition will still be meaningfully interpretable as they will mirror similar relative changes in inhibition observed in the WT background.

Secondly, K_{ATP} channels are more sensitive to inhibition by TNP-ATP than by ATP. Again, this means that any conclusions we draw from experiments measuring relative changes in binding and inhibition rely on those relative changes affecting ATP binding and inhibition to a similar extent. To try and ameliorate these caveats

as best as we can, where possible we have performed control experiments in the WT background with ATP to ensure that introduced mutations result in similar relative effects on nucleotide binding and inhibition despite the background of the construct or the identity of the nucleotide. As control experiments of this sort are not possible in unroofed membranes, where it is impossible to measure current inhibition, we have focused on patch-clamp fluorometry for constructs where expression is good enough to measure sufficient fluorescence.

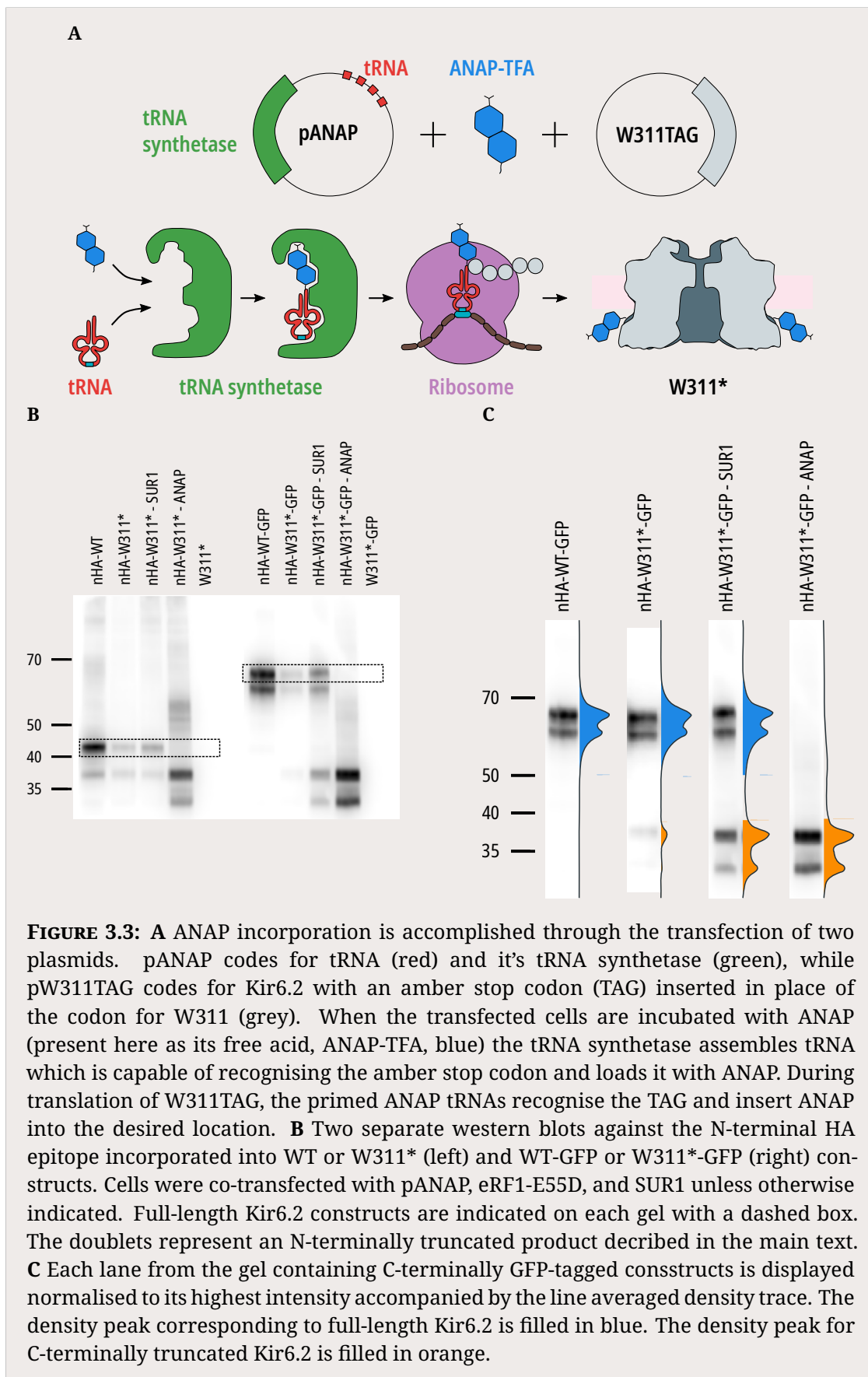
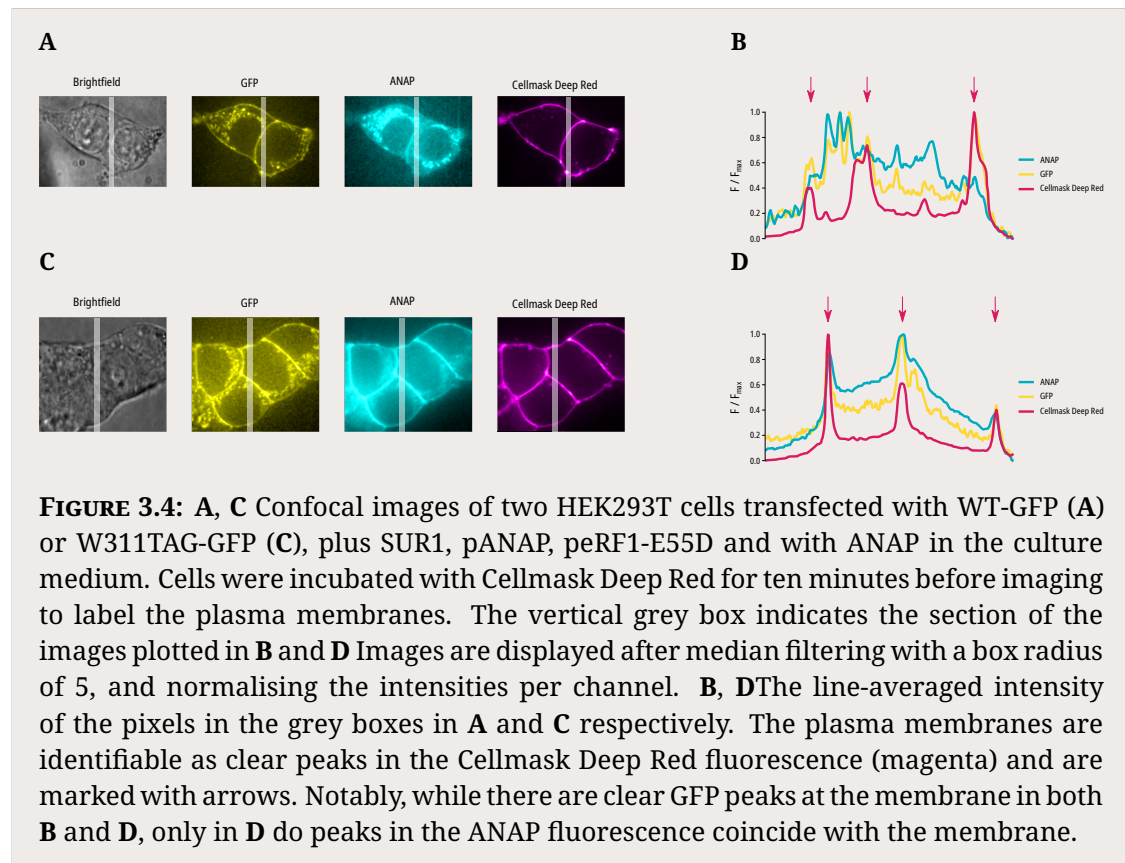
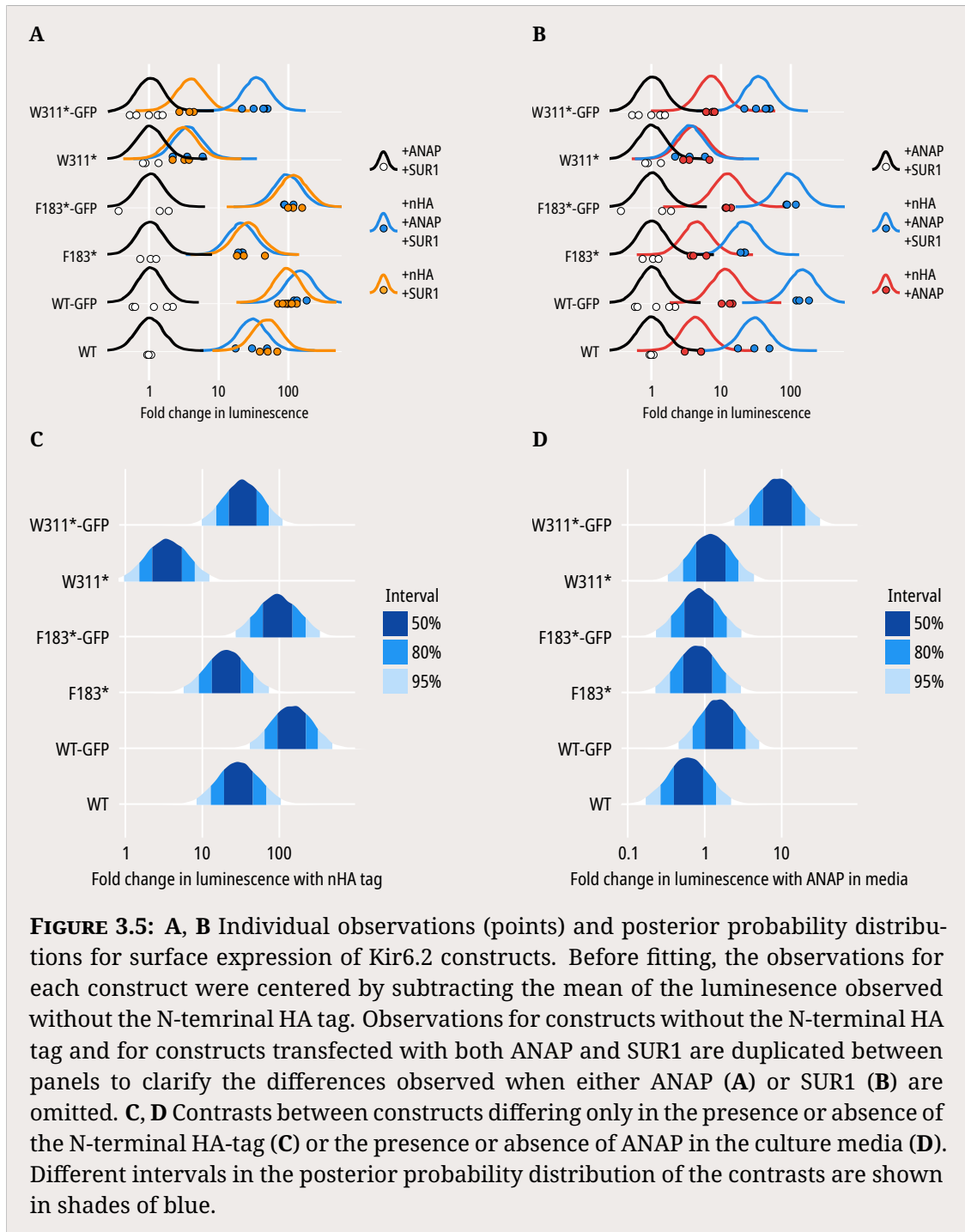
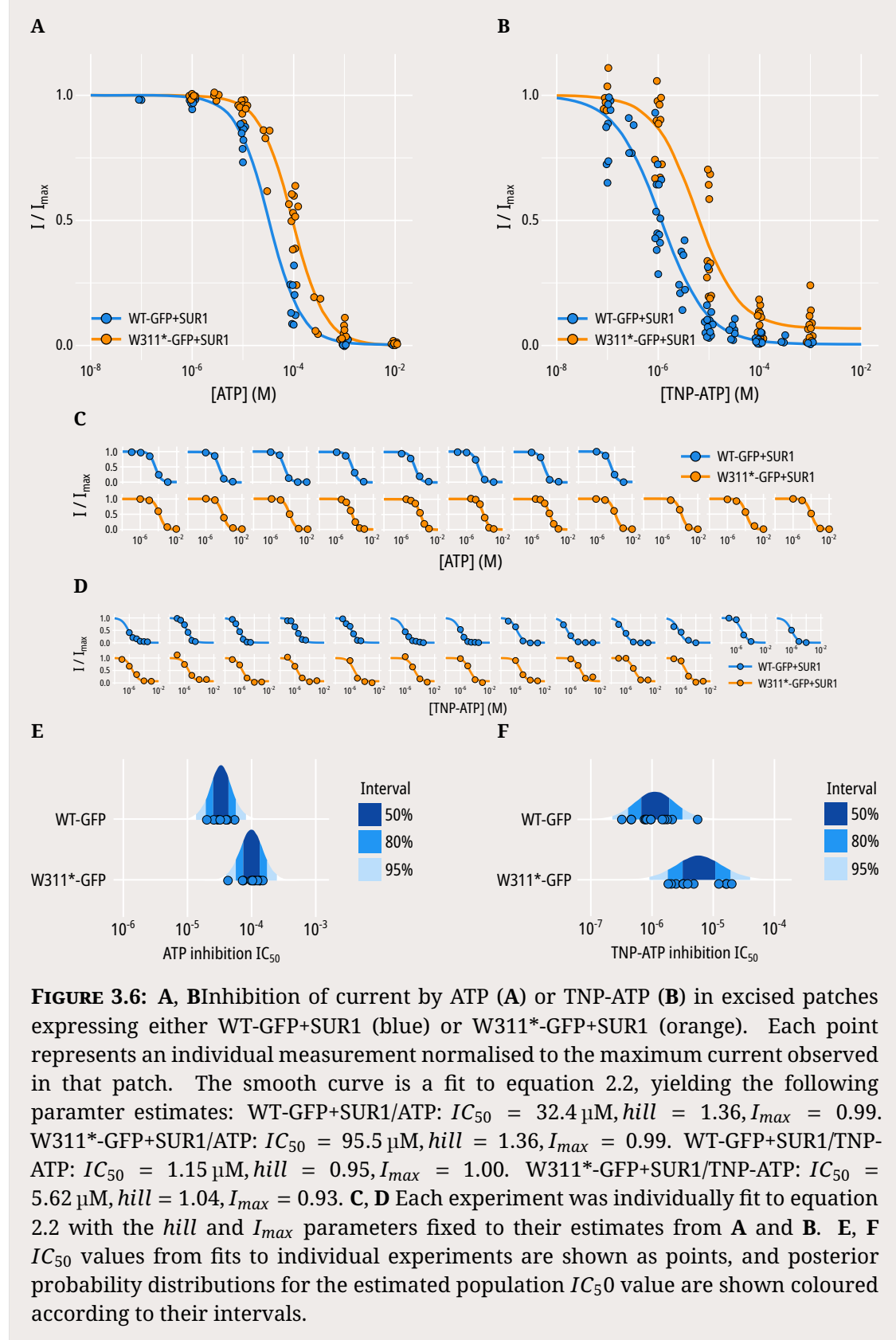
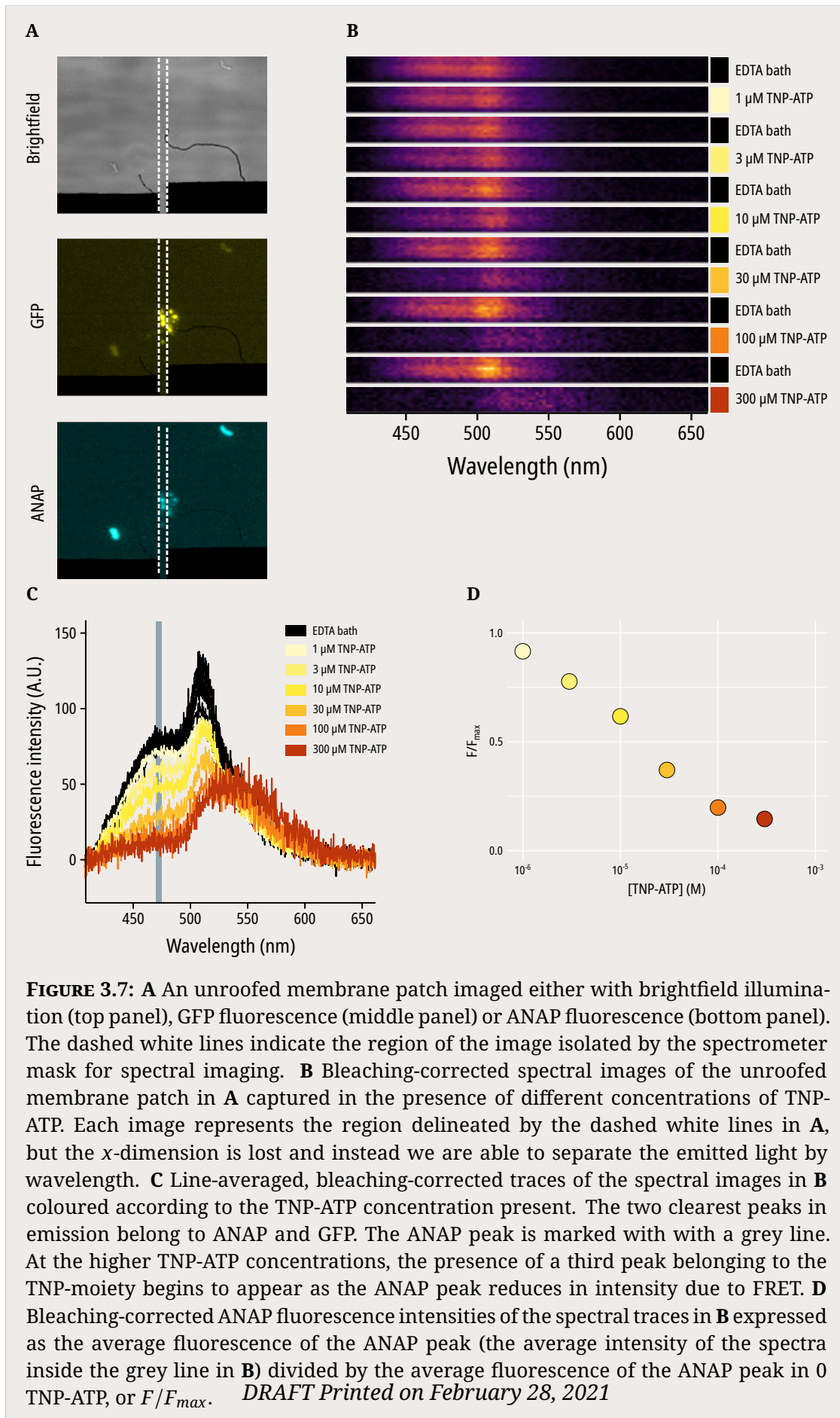


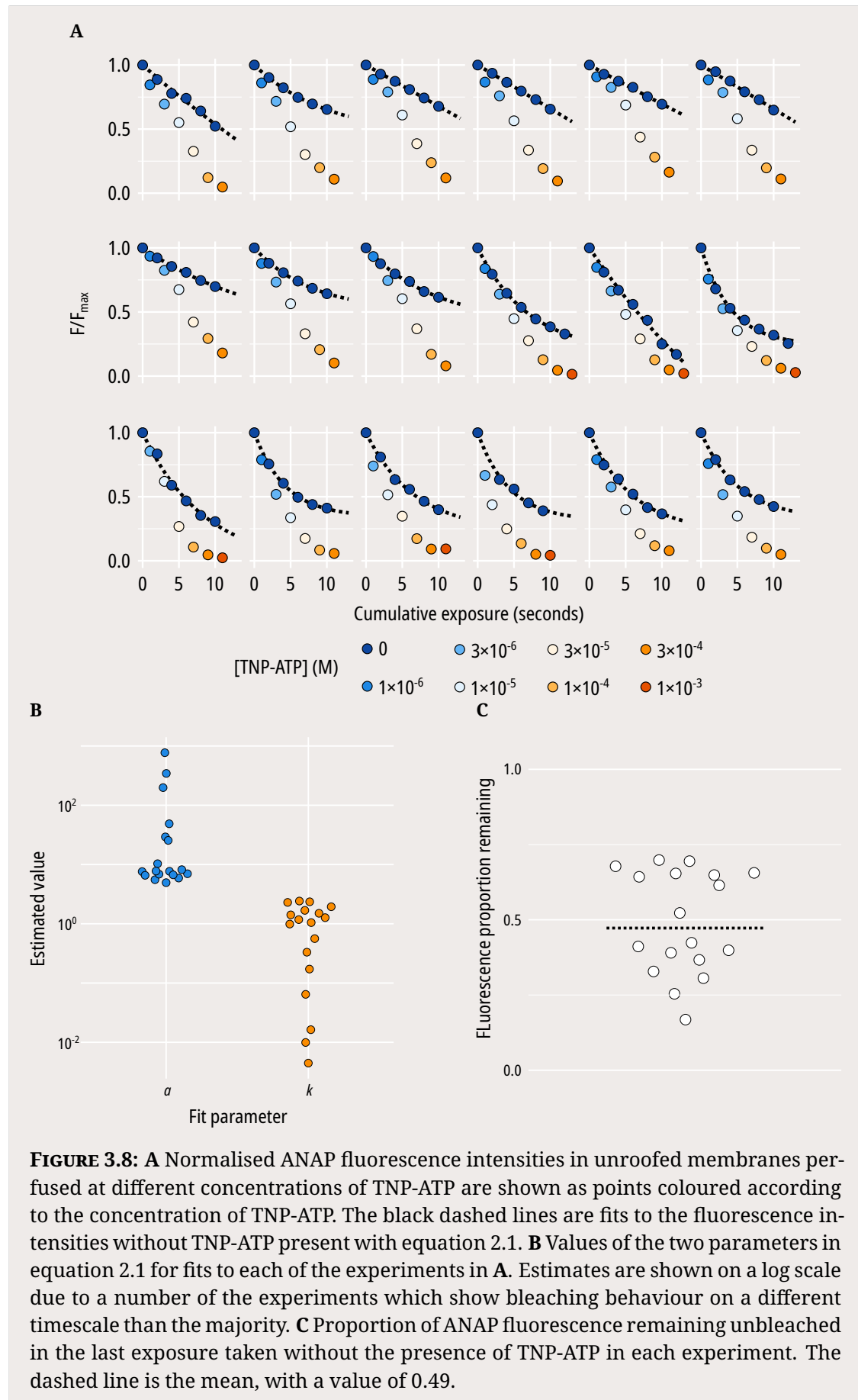
FIGURE 3.3: **A** ANAP incorporation is accomplished through the transfection of two plasmids. pANAP codes for tRNA (red) and its tRNA synthetase (green), while pW311TAG codes for Kir6.2 with an amber stop codon (TAG) inserted in place of the codon for W311 (grey). When the transfected cells are incubated with ANAP (present here as its free acid, ANAP-TFA, blue) the tRNA synthetase assembles tRNA which is capable of recognising the amber stop codon and loads it with ANAP. During translation of W311TAG, the primed ANAP tRNAs recognise the TAG and insert ANAP into the desired location. **B** Two separate western blots against the N-terminal HA epitope incorporated into WT or W311* (left) and WT-GFP or W311*-GFP (right) constructs. Cells were co-transfected with pANAP, eRF1-E55D, and SUR1 unless otherwise indicated. Full-length Kir6.2 constructs are indicated on each gel with a dashed box. The doublets represent an N-terminally truncated product described in the main text. **C** Each lane from the gel containing C-terminally GFP-tagged constructs is displayed normalised to its highest intensity accompanied by the line averaged density trace. The density peak corresponding to full-length Kir6.2 is filled in blue. The density peak for C-terminally truncated Kir6.2 is filled in orange.











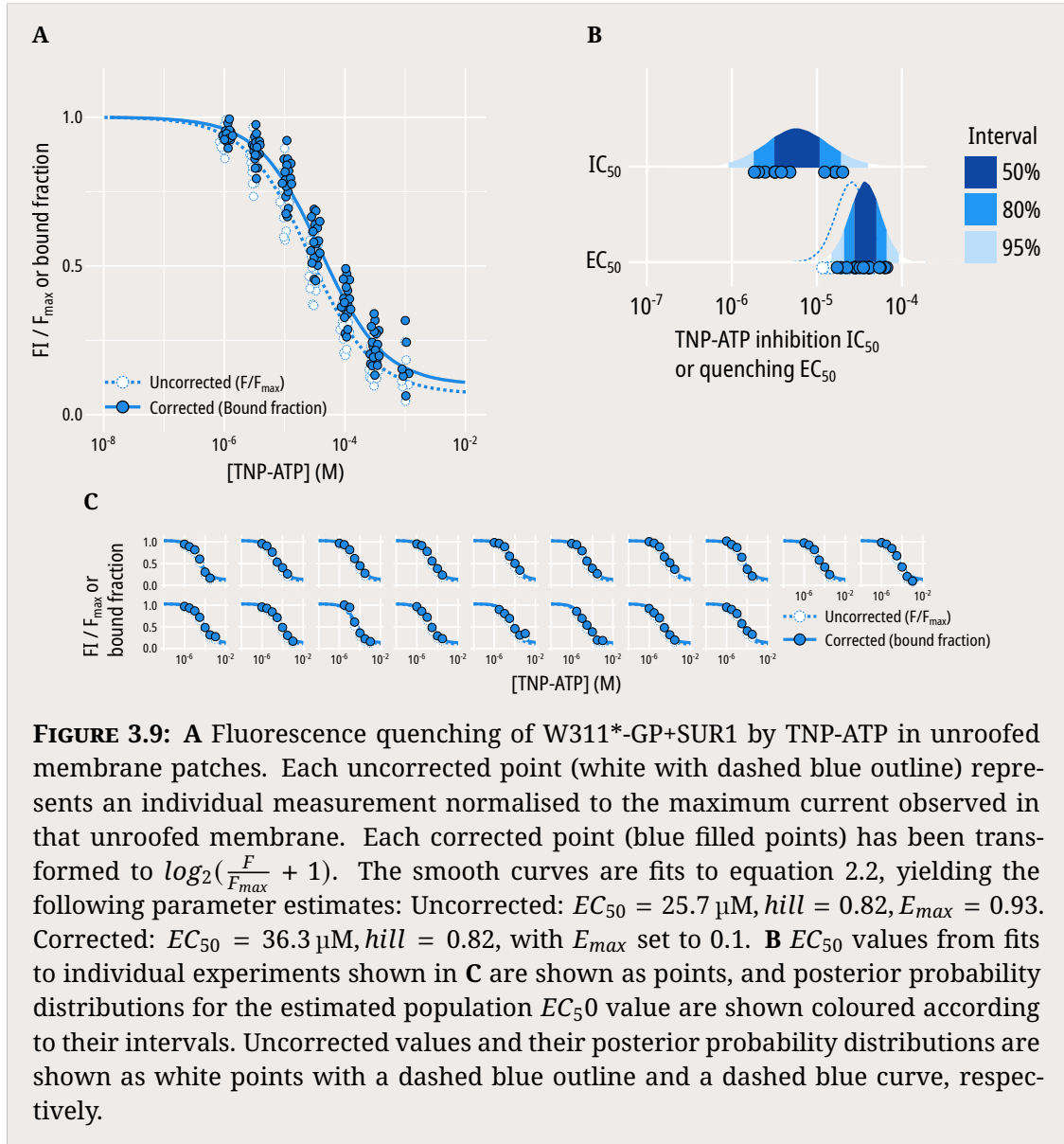
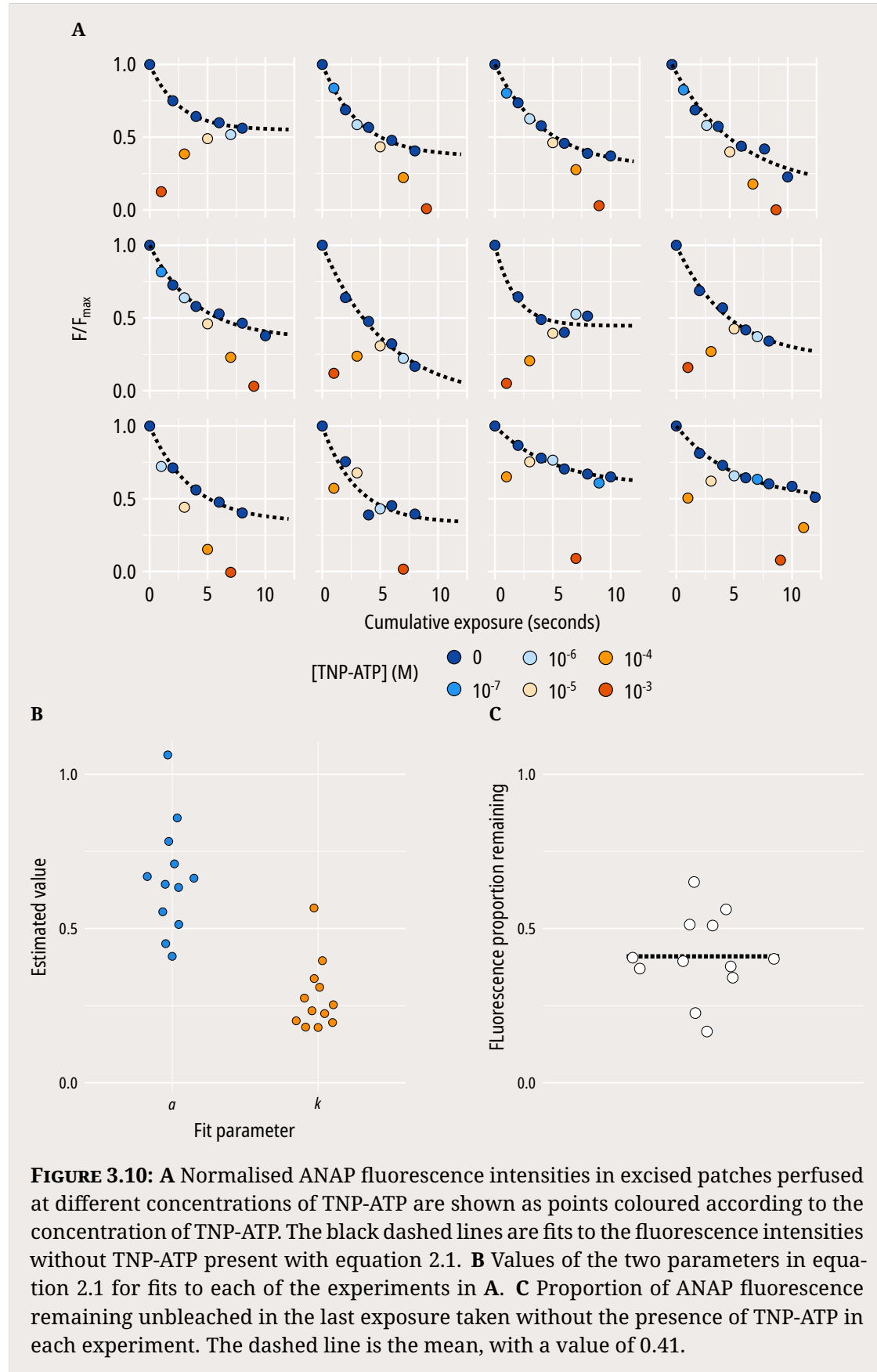
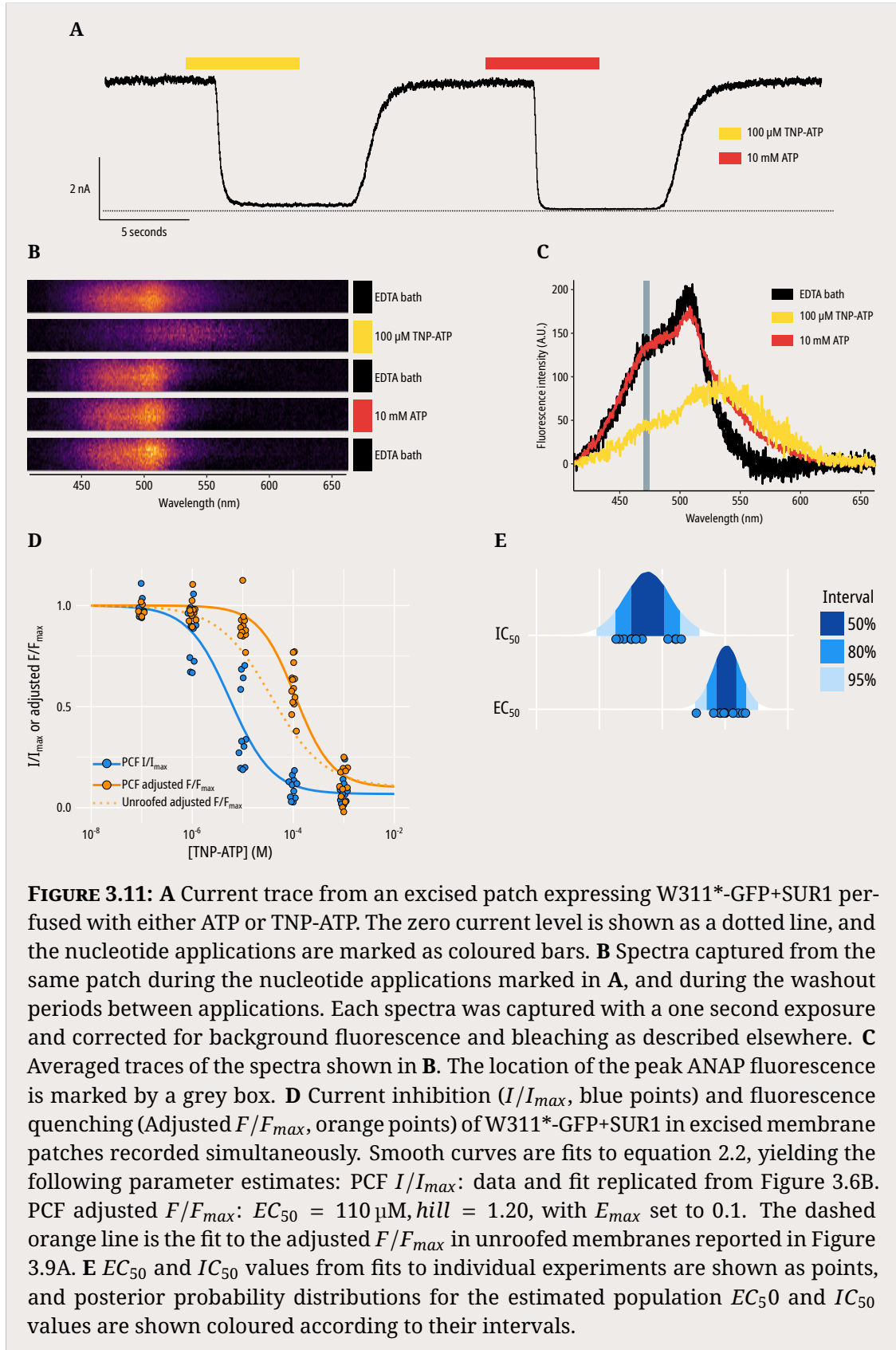


FIGURE 3.9: **A** Fluorescence quenching of W311*-GP+SUR1 by TNP-ATP in unroofed membrane patches. Each uncorrected point (white with dashed blue outline) represents an individual measurement normalised to the maximum current observed in that unroofed membrane. Each corrected point (blue filled points) has been transformed to $\log_2(\frac{F}{F_{max}} + 1)$. The smooth curves are fits to equation 2.2, yielding the following parameter estimates: Uncorrected: $EC_{50} = 25.7 \mu\text{M}$, hill = 0.82, $E_{max} = 0.93$. Corrected: $EC_{50} = 36.3 \mu\text{M}$, hill = 0.82, with E_{max} set to 0.1. **B** EC_{50} values from fits to individual experiments shown in **C** are shown as points, and posterior probability distributions for the estimated population EC_{50} value are shown coloured according to their intervals. Uncorrected values and their posterior probability distributions are shown as white points with a dashed blue outline and a dashed blue curve, respectively.





4

MWC modelling

Contents

4.1 Modelling of ion channel function	43
4.1.1 Restricting the subset of possible models	43
4.1.2 Considerations for fitting a model	43
4.1.3 Determining open probability	43
4.2 Implementing an MWC model	49
4.2.1 A simple case	49
4.2.2 The role of PIP ₂	49

4.1 Modelling of ion channel function

4.1.1 Restricting the subset of possible models

4.1.2 Considerations for fitting a model

4.1.3 Determining open probability

Measuring the open probability of an ion channel is most accurately accomplished by single-channel electrophysiological recordings, which allows direct measurement of the time a channel spends in an open state. This approach does not allow for the determination of the open probability of a population of channels great than 2/3 at a time, as it becomes increasingly difficult to separate the openings of different

channels in the population. Thus it would not be possible to determine single channel open probability simultaneously with nucleotide binding, as the fluorescence signal from a small number of channels would be impossible to resolve.

Another approach is noise analysis of currents from large populations of channels. The 'noise' in noise analysis refers to current fluctuations which occur when recording from a population of ion channels due to the stochastic channel gating of individual channels. If there are a constant number of channels (N) which are gated independently from each other and share a homogenous open probability (P_O) and a single open conductance level (i), the observed macroscopic current level I can be described by equation 4.1:

$$I = iNP_O \quad (4.1)$$

and the observed variance of the macroscopic current can be described by the variance of the binomial distribution, equation 4.2:

$$\sigma^2 = NP_O \cdot (1 - P_O) \cdot i^2 \quad (4.2)$$

where the single channel current is essentially a scaling factor. If we assume that in a given recording N and i remain constant, and it is P_O which changes in response to any given stimuli, then we can combine equations 4.1 and 4.2 to yield equation 4.3:

$$\sigma^2 = iI - \frac{1}{N} \cdot I^2 \quad (4.3)$$

This equation yields a parabola from $I = 0$ to $I = Ni$. Intuitively, there can be no variance when P_O is exactly 0 or 1, as there will be no opening or closing events which can give rise to current fluctuations. Once i and N have been determined for a given experiment, the observed current magnitude I can be converted into the P_O for the population of channels by rearranging equation 4.1 as follows:

$$P_O = \frac{I}{iN} \quad (4.4)$$

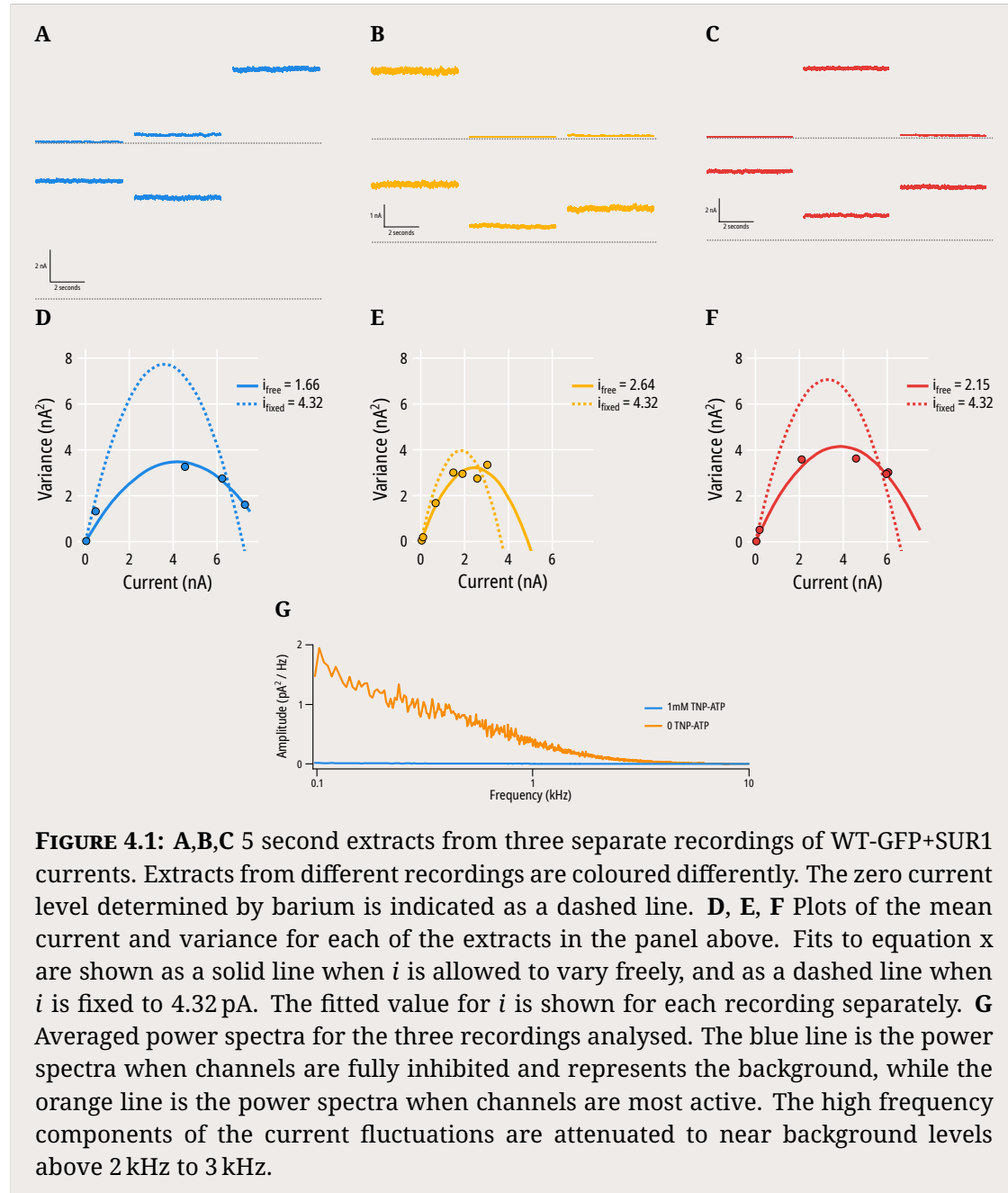
Equation 4.3 can be fit to experimental data by calculating the variance of observed current at different current magnitudes. This calculation is not exactly

trivial, and has been accomplished a number of different ways for different purposes. For channels with fast inactivation such as the Na_v family, non-stationary noise analysis involves repeating a stimulus multiple times and measuring variance as the squared sum of deviations from the mean of the current magnitude calculated at the same time point across multiple stimuli, referred to in the literature as an 'isochrone'. For channels which do not inactivate, stationary noise analysis is possible, and variance can be measured as the squared sum of deviations from the mean current magnitude over a period of time for which I is 'stationary' (Figure 4.1A, 4.1B, 4.1C).

Stationary noise analysis has been described for K_{ATP} channels before by a number of different researchers (Shyng, Paolo, Peter). Unfortunately, in most of the published research the exact procedure for extracting the parameters in equation 4.2 is described in the methods section, but the quality of the fits and the value of the fitted parameters besides the final calculated P_O is not discussed. A notable exception to this rule is (Paolo), in which two findings are discussed. Firstly, fitting equation 4.3 to the mean and variance of 200 ms sections of macroscopic currents from wild-type Kir6.2+SUR2A resulted in a systematic underestimation of the single channel current i . From single channel experiments, the single channel current was determined to be 4 pA, while the value obtained from fitting macroscopic currents was only 2 pA. In the case of WT-GFP+SUR1, we see a similar underestimation of single channel current (Figure 4.1D, 4.1E, 4.1F), with fits yielding estimates of 1.66 pA to 2.64 pA, while measured single channel currents are at least 4 pA. This underestimate of i is most likely due to an underestimate of channel current variance as P_O increases, which could be due to two main reasons.

Firstly, the process of filtering and digitising channel currents can lead to underestimates of variance depending on the relationship between the open time of the measured channel and the cut-off frequency of the filter used. It is unlikely that this phenomenon is responsible for our findings, as the K_{ATP} mean open time duration is close to 1 ms and filtering at 5 kHz would lead to less than a 5 % underestimation of i . Even if the mean open time of WT-GFP+SUR1 was closer to 0.1 ms, we would expect a 20 % reduction rather than the 50 % we actually observe. Empirically, we

can use the frequency power spectrum of our measured current fluctuations to determine whether there may be high frequency channel openings we are missing (Figure 4.1G). For WT-GFP+SUR1, we observe that at frequencies approaching our filter cut-off at 5 kHz there is very little observed amplitude in active channels when compared to fully inhibited channels, suggesting we are not missing high frequency current fluctuations.



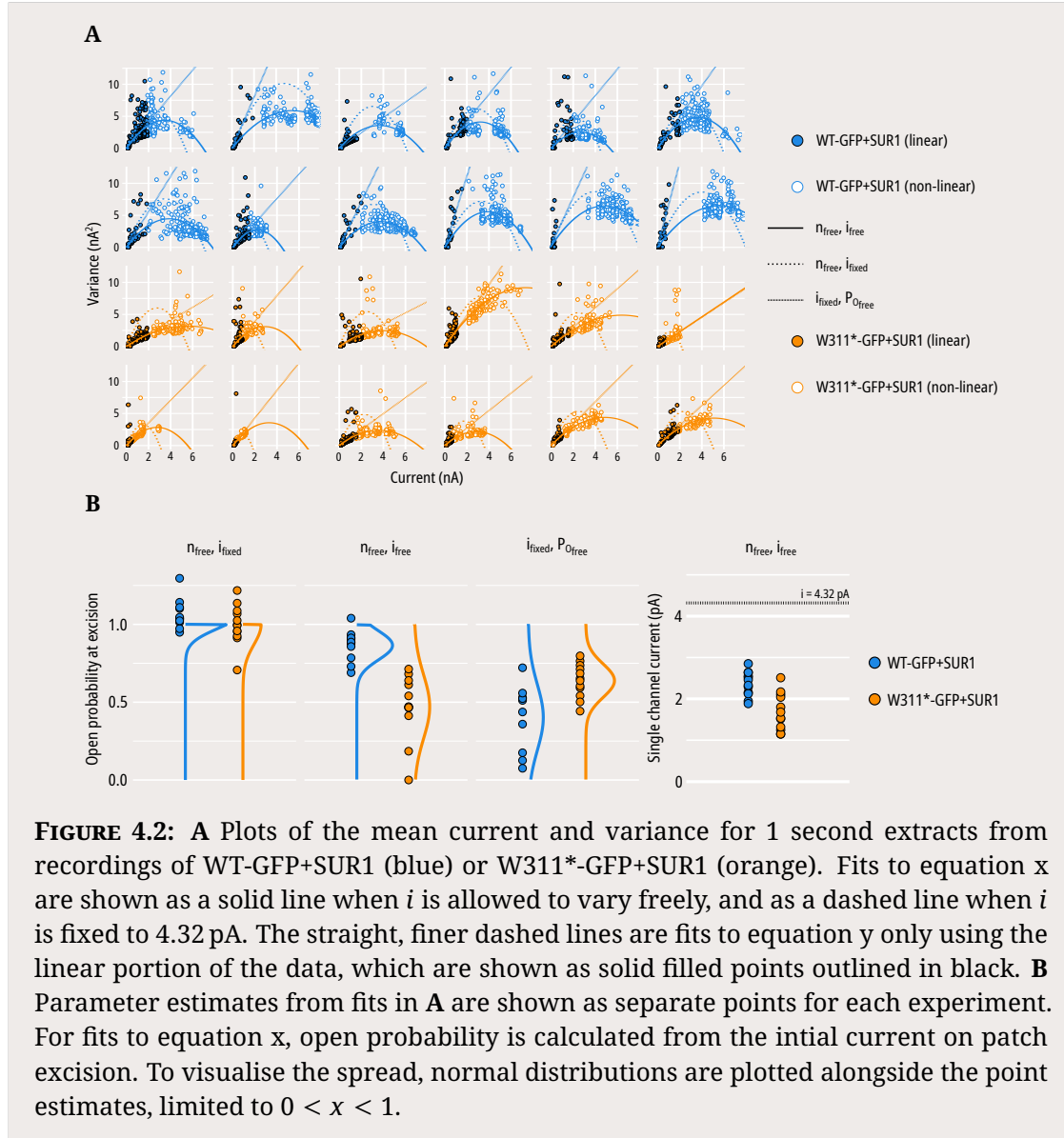
Secondly, an underestimation of i could occur due to violations in the underlying assumptions of the binomial distribution. The first two assumptions are that N and i are constant throughout a recording. We know that i does not change on nucleotide inhibition of K_{ATP} channels, nor is it affected by PIP₂ and rundown. Additionally, in excised patches it is improbable that there will be any change in N during the course of a recording. The third assumption is that the channels in a patch share a homogenous P_O , which exhibits graded changes in response to stimuli (in our case, application of nucleotide). This assumption is far harder to justify for our experimental condition, in which channel rundown due to loss of PIP₂ results in a complicated mixture of channel populations with different P_O s.

An extreme case in which channels transition between two states, one where $0 < P_O < 1$ and one where $P_O \approx 0$ can be approximated by equation 4.2, with a channel transitioning to the $P_O \approx 0$ state essentially considered to be no longer available to open, thus reducing N . Thus, fitting the observed current-variance data with 4.2 would yield a straight line where the slope of the line is equal to $i \cdot (1 - P_O)$. This formulation of equation 4.2 has been used successfully in the analysis of currents from CRAC channels, VSOA channels, and in the analysis of a specific cardiac K_{ATP} channel mutation. Unfortunately, in our case channel rundown does not render the K_{ATP} channel completely unable to open, with fully rundown channels displaying single channel open probabilities in the range of 0.05 to 0.25. Instead of each current measurement being a draw from a single binomial distribution, we are instead drawing from a mixture of binomial distributions with different P_O s. We can demonstrate how this leads to an underestimation of i by simulating a simple case where there are two populations of channels, a and b , one with a tenfold lower P_O than the other. By superimposing a stimulus which reduces P_O by an equal factor in both populations.

$$N_a + N_b = 1000$$

$$0 < P_{O_a} < 1 \quad (4.5)$$

$$P_{O_b} = \frac{P_{O_a}}{10}$$

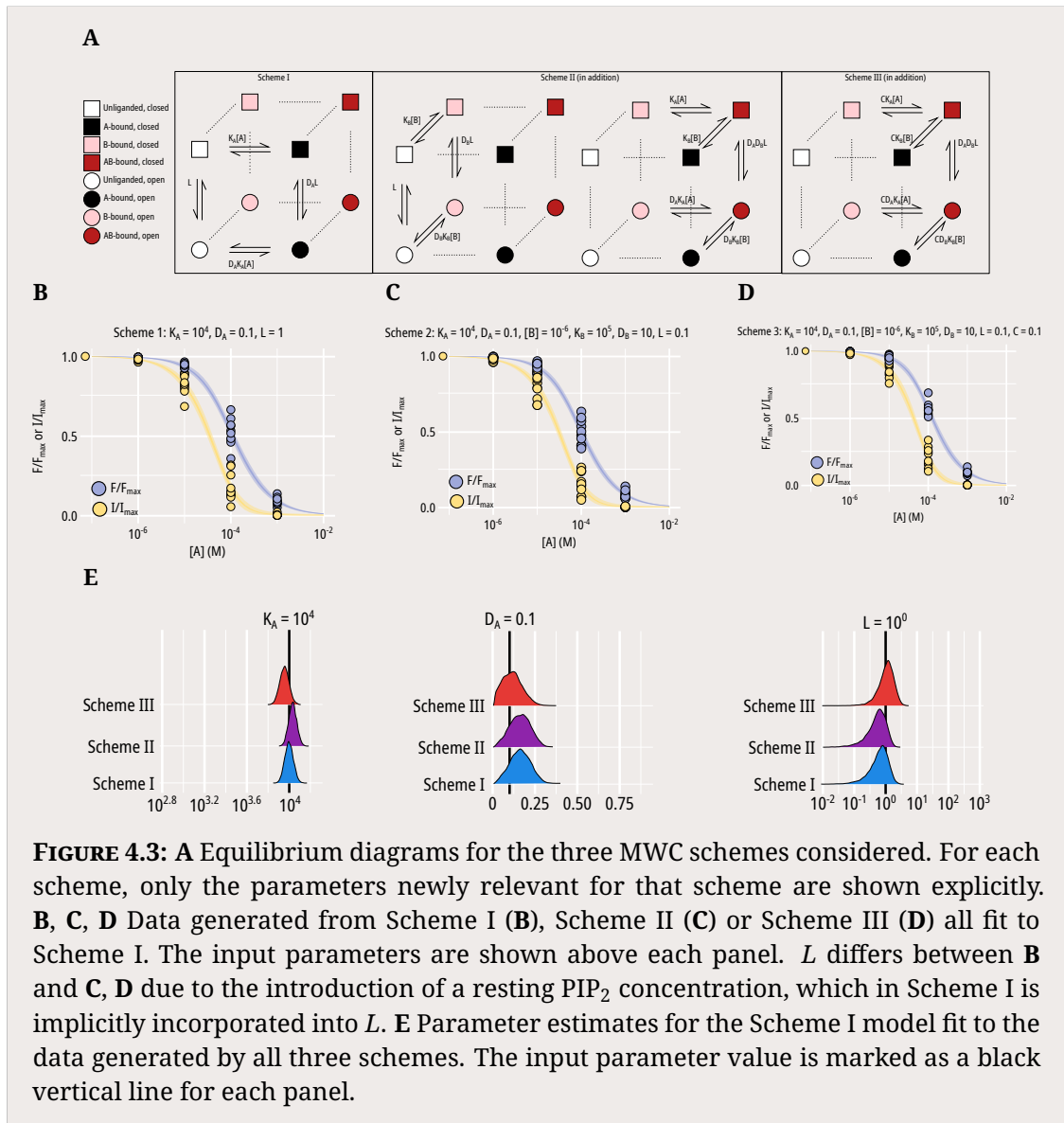


4.2 Implementing an MWC model

4.2.1 A simple case

The simplest case of an allosteric MWC model for an ion channel is shown as Scheme I in Figure 4.3A. This simple case assumes a channel composed of a single monomer with a single binding site for ligand A . The channel is restricted to two states, open and closed. These two states exist in an equilibrium described by L , which is equivalent to $\frac{[open]}{[closed]}$. Ligand A binds to the protein with a microscopic affinity

constant K_A . The ligand A differentially stabilises the open and closed states by a constant D . When D is unity, the ligand A binds equally to both states and so does not influence the conformational changes of the channel. When $D > 1$, the ligand A preferentially stabilises the open state, while when $D < 1$ the ligand instead preferentially stabilises the closed state.



4.2.2 The role of PIP₂

If we consider introducing a second ligand B which binds to a distinct site on the same monomer and does not directly interact with ligand A, we introduce the states shown in Scheme II of Figure 4.3A. Each ligand has its own microscopic association constant (K_A or K_B) and its own preference for the open or closed states (D_A or D_B). Importantly, there is no interaction term between ligand A and ligand B; the only way the binding of the ligands can impact each other is through effects on L . Scheme II is therefore a restricted form of scheme III, which explicitly introduces a term for local interaction (C) between binding sites for ligands A and B on the same monomer. When C is unity, Scheme III becomes Scheme II. When $C < 1$, binding of one ligand reduces the ability of the other ligand to bind on the same monomer. When $C > 1$, binding of one ligand enhances the ability of the other ligand to bind on the same monomer.

To study nucleotide binding to Kir6.2, I have used Scheme I (expanded to incorporate four identical monomers) as an approximation of the K_{ATP} channel, with ligand A representing nucleotides. To determine whether this approximation is appropriate, I generated data using each of the three schemes as the underlying model of channel function and then fit the generated observations to Scheme I (Figure 4.3B, 4.3C, 4.3D). Ten individual sets of observations were generated using the inputs shown above each figure panel as the centre of a lognormal distribution with a standard deviation of 0.25. These observations were then fit to Scheme I (as done previously throughout the thesis) and the values of the three free parameters (K_A , D_A and L) were estimated (Figure 4.3E).

We know that Scheme I is only an approximation of nucleotide binding as it does not explicitly include PIP₂. The question is, if the underlying data generating model is Scheme II which explicitly includes a second ligand, are we still able to extract meaningful parameter estimates by fitting the observed data to Scheme I? In addition, to date it remains unclear whether there is local allosteric between the nucleotide and PIP₂ binding sites. The existence of local allosteric would mean that Scheme III, which includes an explicit term for this interaction, would best

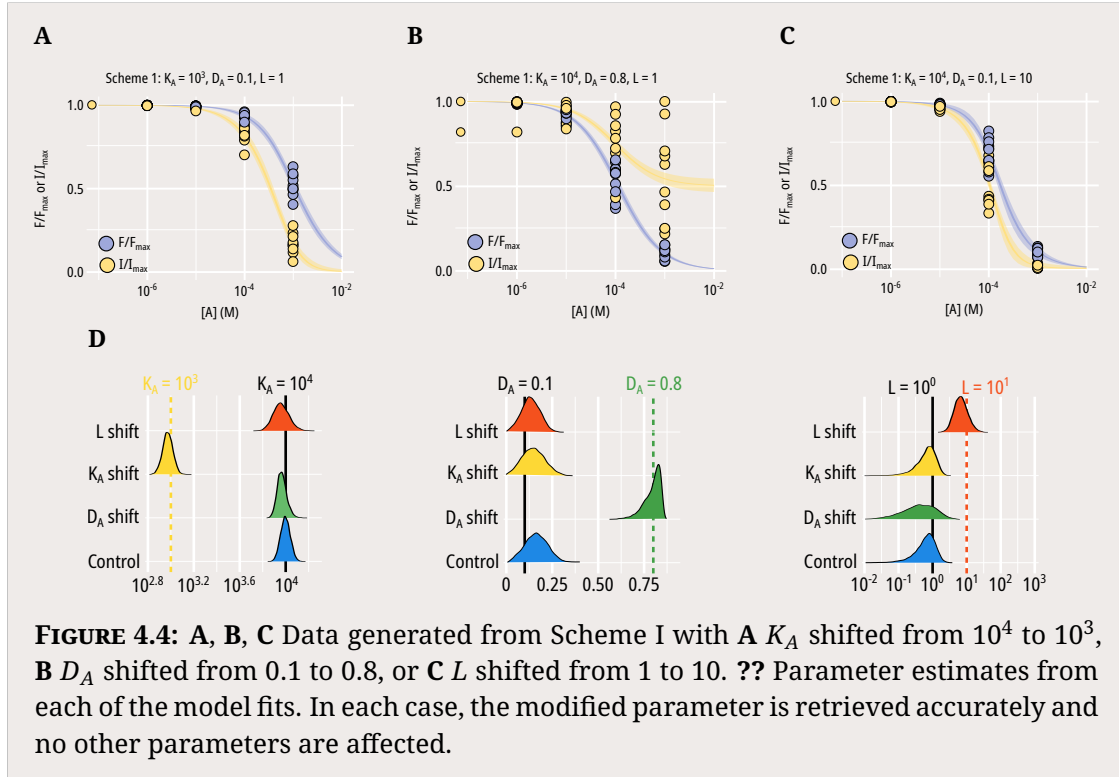


FIGURE 4.4: **A, B, C** Data generated from Scheme I with **A** K_A shifted from 10^4 to 10^3 , **B** D_A shifted from 0.1 to 0.8, or **C** L shifted from 1 to 10. ?? Parameter estimates from each of the model fits. In each case, the modified parameter is retrieved accurately and no other parameters are affected.

represent the true data generating model. We can show that even when Scheme II or Scheme III are the underlying data generating model, with ligand *B* representing PIP₂, we are still able to extract the true values of K_A and D_A by fitting the generated data to Scheme I (Figure 4.3). Parameter choices for Scheme II and III are such that the open probability of the channel at 0 [ATP] is still 50%, equivalent to $L = 1$ in Scheme I. I really need to redo this with the true L set to 0.01 instead of 0.1 as that is closer to post rundown open probability...

We can also show that when Scheme I is the underlying data generating model, changes in any of the three parameters are easily identified and retrieved by fitting the observed data to Scheme I (Figure 4.4). This suggests that introducing mutations which directly effect any of the three parameters of this model would be easily identifiable if Scheme I was the true underlying model.

What if Scheme II or III were the underlying model? We would still expect changes in the three parameters which exist in Scheme I to be identifiable (I should probably check this), although L would not represent the true unliganded open/closed

equilibrium as we would be estimating an L modified by the resting PIP₂ concentration, K_B , D_B and C - in this case, the estimated L parameter in fact represents the ATP-unbound open/closed equilibrium.

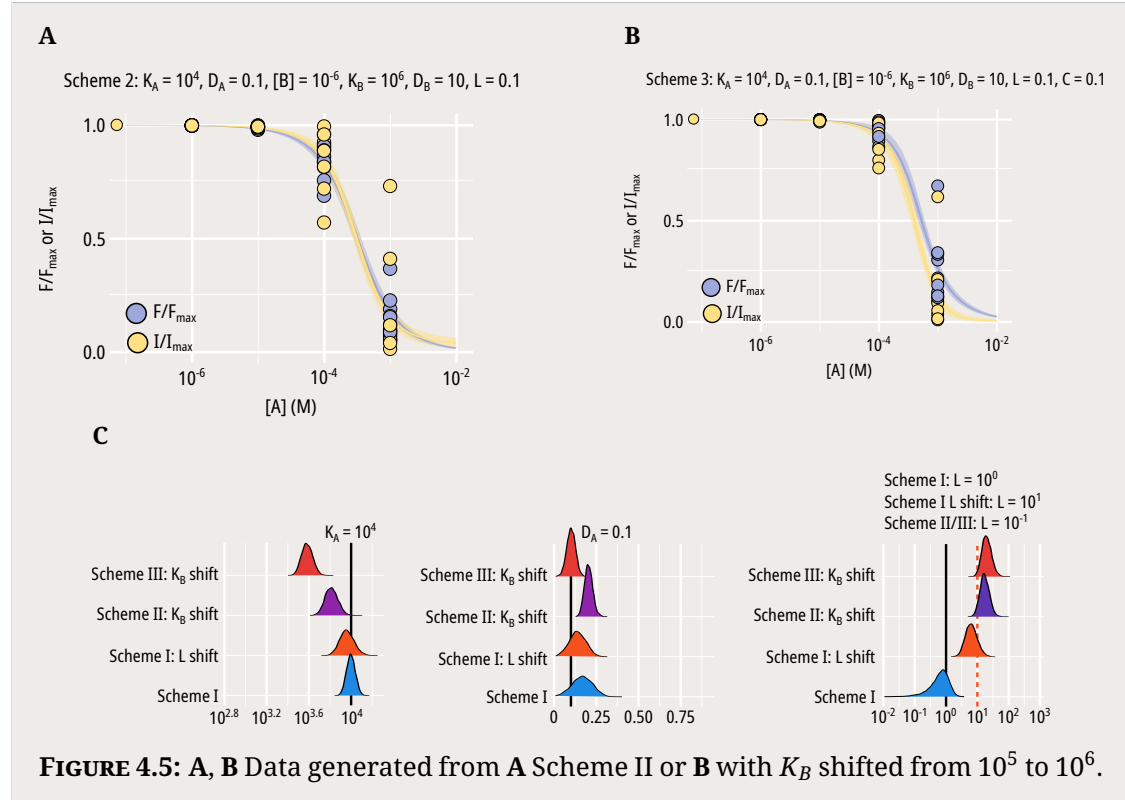


FIGURE 4.5: A, B Data generated from **A** Scheme II or **B** with K_B shifted from 10^5 to 10^6 .

However, it is unclear how changes in parameters which are not explicitly modelled in Scheme I will affect the generated data and the parameter estimates obtained by fitting the data to Scheme I. Figure 4.5 shows the results of increasing K_B by tenfold on data generated from Scheme II (Figure 4.5A) or Scheme III (Figure 4.5B). The first observation of note is that the generated data closely resemble those generated from Scheme I when L is increased (Figure 4.4C), and indeed when the L parameter estimates for a tenfold shift in K_B in Scheme II/III and tenfold shift in L for Scheme I are compared (Figure 4.5C, right panel) are compared they appear to be similar. So far so good, as an observed increase in L when fit with Scheme I would lead us to draw the correct inferences about changes in the underlying model (i.e. the open probability of the cnall has indeed increased). However, changes in K_B are not perfectly captured by changes in L when fit to scheme I. Notably, if local

allostery exists between the nucleotide and PIP₂ binding site - if Scheme III is the true underlying model - then fitting the observed data to Scheme I would lead us to estimate an incorrect value for K_A (Figure 4.5A). Thus, if there is local allosteric coupling between the sites, then a mutation which induces an increase in the binding affinity for PIP₂ would not just increase our estimate of L (which would lead to a correct inference) but it would also decrease our estimate of K_A by a non-insignificant amount, which could lead to the incorrect inference that a mutation is causing a direct change in nucleotide binding when it is in fact causing a direct change in PIP₂ binding, which through local allosteric coupling is influencing our estimates of K_A .

5

Nucleotide regulation of Kir6.2

Contents

5.1 Nucleotide binding	55
5.1.1 G334D abolishes nucleotide binding	55
5.2 Channel gating	55
5.2.1 C166S alters inhibition without affecting binding	55
5.2.2 Mutations at E179 alter both inhibition and binding	55
5.2.3 Mutations at K39 alter both inhibition and binding	55
5.3 Discussion	55

5.1 Nucleotide binding

5.1.1 G334D abolishes nucleotide binding

5.2 Channel gating

5.2.1 C166S alters inhibition without affecting binding

5.2.2 Mutations at E179 alter both inhibition and binding

5.2.3 Mutations at K39 alter both inhibition and binding

5.3 Discussion

6

Regulation of Kir6.2 by SUR1

Contents

6.1 Intrinsic effects of SUR1	58
6.1.1 SUR1 alone alters nucleotide inhibition	58
6.1.2 Presence of SUR1 alone does not alter apparent nucleotide binding	58
6.1.3 Presence of SUR1-TMD0 alone does not alter apparent nucleotide binding	58
6.2 SUR1 an nucleotide regulation	58
6.2.1 Mutations at SUR-K205 alter nucleotide binding and inhibition	58
6.2.2 THe presence of magnesium does not affect nucleotide binding	58
6.3 Discussion	58

6.1 Intrinsic effects of SUR1

- 6.1.1 SUR1 alone alters nucleotide inhibition**
- 6.1.2 Presence of SUR1 alone does not alter apparent nucleotide binding**
- 6.1.3 Presence of SUR1-TMD0 alone does not alter apparent nucleotide binding**

6.2 SUR1 an nucleotide regulation

- 6.2.1 Mutations at SUR-K205 alter nucleotide binding and inhibition**
- 6.2.2 THe presence of magnesium does not affect nucleotide binding**

6.3 Discussion

7

Discussion

Appendices

